Label-free lymphocytes reconstitution using side scatter for optimal T cell manufacturing

Tongjin Wu[1], Yen Hoon Luah[1], Yongqiang Luo[1], Howard John Womersley[1], Lih Feng Cheow[1,2,*]

[1]Department of Biomedical Engineering, Faculty of Engineering, National University of Singapore, Singapore 117583, Singapore.

[2]Institute for Health Innovation and Technology, National University of Singapore, Singapore 117599, Singapore.

[*]Correspondence: lihfeng.cheow@nus.edu.sg

SUMMARY

Lymphocyte biology research commonly involves purification of lymphocyte subpopulations by fluorescence-activated cell sorting (FACS) or immunomagnetic separation (IMS), both of which typically rely on antibody labeling of validated cell markers. Methods enabling label-free segregation of lymphocyte subpopulations would be invaluable with regard to less-perturbation, simplicity and cost-effectiveness. Here, we introduce TRuST, a label-free approach for T cell reconstitution using side-scatter (SSC). TRuST-sorted SSC^{low} cells enrich for $CD4^+$ T and naïve T cells, while SSC^{high} cells enrich for $CD8^+$ T, NK and differentiated T cells. Enrichment purity can be improved by computational gate design. SSC^{low} cells have superior expansion capacity and generate more central memory precursors with naïve-resembling cytokine responses. Moreover, we find that both T cell differentiation status and CD4/CD8 T ratio in the starting cellular material are critical attributes predicting T cell product quality and quantity. TRuST presents an effective and reliable technique for label-free lymphocytes selection and reconstitution.

Keywords: flow cytometry; side scatter; antibody-free; label-free; cell type purification; T cell reconstitution; naïve T cell enrichment; ratio of CD4/CD8 T; T cell manufacturing

INTRODUCTION

Lymphocytes, mainly including T cells, natural killer (NK) cells and B cells, play an indispensable part in human immune system. Use of purified lymphocyte subsets for

lymphocyte biology research is critical to dissect the functional heterogeneity of lymphocyte subpopulations. Fluorescence-activated cell sorting (FACS) (Cossarizza et al., 2019) and immunomagnetic separation (IMS) (Plouffe et al., 2015) are methods of choice to obtain purified cell types of interest, relying on the labeling with specific antibody conjugates such as fluorochrome-modified antibodies and magnetic beads-coupled antibodies. Despite powerful of these technologies, there still exist some limitations.

One of the most common concerns is antibody labeling-caused functional change of immune cells which are relatively sensitive to antibody-mediated activation/inhibition (Attanasio and Wherry, 2016; Chen and Flies, 2013), interfering with downstream cell biology studies. Thus, careful selection of validated antibody clones and strict experimental controls are generally required in experimental design. In addition, it is extremely difficult to release the bound fluorescent antibodies on cell surface if cell viability was to be maintained. These sorted cells are not suitable for re-labeling with the same fluorochrome conjugates due to occupancy of fluorescence channels, resulting in less flexibility in the choice of fluorescent antibodies for multiparametric flow cytometry experiments. Also, these cells might not be feasible for downstream cell culture assays if the occupied target markers were necessary to be re-engaged for cell functionality. For example, the labeling of CD3 receptor for T cells enrichment by FACS might affect the activation/expansion of T cells when CD3/CD28 engagement is required for cell stimulation (Roddie et al., 2019). Superparamagnetic particles-

antibody coupling technique combined with magnetic isolation is shown to be capable of minimizing the effects introduced by fluorescent antibodies occupancy thanks to its effective separation with only unsaturated concentration of bead-antibody conjugates (Grutzkau and Radbruch, 2010; Plouffe et al., 2015). However, concerns arising from the use of nanosized magnetic beads include internalization of magnetic beads and preservation of magnetic properties for an extended period in cells that are subjected to limited proliferation, which calls for caution when repetitive positive isolation steps after in vitro culture are required (Laghmouchi et al., 2020; Teeman et al., 2019). More recently, Miltenyi Biotec has introduced the REAlease Fluorochrome Technology that relies on engineered antibody fragments with low epitope binding affinities which allows stained antibodies to be released. Design of releasable superparamagnetic beads-antibody conjugate could be of interest to improve magnetism-based cell separation. Nevertheless, the time and cost for sample processing are inevitably increased and concerns relating to cell labeling-caused alteration on downstream assays still exist. Therefore, with regard to less perturbation on target cells and enhanced flexibility in sample processing, approaches that enable label-free cell type separation from mixed lymphocytes would be highly attractive and great useful in lymphocyte biology studies.

Selection of specific T cell types has also seen its utility in the field of cellular immunotherapy. Insight into attributes of therapeutic potency based on T cell receptor (TCR)-redirected T cells such as chimeric antigen receptor (CAR) T cells and TCR-T

cells is a central goal of T cell immunotherapy (Majzner and Mackall, 2019; Rafiq et al., 2020). The quality of T cell products generated ex vivo has been recognized as a critical factor affecting immunotherapy efficacy (Deng et al., 2020; Finney et al., 2019; Fraietta et al., 2018; Roddie et al., 2019). Unfractionated peripheral blood mononuclear cell (PBMC) concentrates are commonly used for T cell production, leading to uncontrollable batch-to-batch variation. Separate expansion of $CD4^+$ T and $CD8^+$ T cells pre-enriched by immunomagnetic selection enhances product consistency and manufacturing feasibility (Gardner et al., 2017; Shah et al., 2020; Sommermeyer et al., 2016; Turtle et al., 2016). Of note, $CD4^+$ T cells help is critical for shaping the adaptive immunity of $CD8^+$ T cells in vivo (Nakanishi et al., 2009; Sun et al., 2004) and improves $CD8^+$ T cells tumor-eradicating potency (Alspach et al., 2019; Arina et al., 2017; Nakanishi et al., 2009; Schietinger et al., 2010). However, the notion, whether $CD4^+$ T and $CD8^+$ T cells should be expanded separately or together at designed ratio in vitro, especially in the scenario where external antigens are absent, remains to be clarified. In addition, adoptive transfer of T cell products derived from less-differentiated T cell subsets shows better curative potential than their more-differentiated counterparts as observed in both animal works (Berger et al., 2008; Gattinoni et al., 2011; Hinrichs et al., 2009; Hinrichs et al., 2011; Wang et al., 2011) and clinical studies (Finney et al., 2019; Fraietta et al., 2018; Xu et al., 2014). These studies suggest that preselecting specific T cell subtypes would be very useful for cell manufacturing aiming to improve immunotherapy efficacy. Undoubtedly, increased demand for therapeutic T cell product calls for cost-effectiveness and manufacturing simplicity. Methods enabling the

111 segregation of ideal cell subsets without the use of costly antibodies would be
112 invaluable by omitting the requirement of large amount of clinical grade
113 immunomagnetic antibodies and complicated downstream processing workflows.
114
115 There has been an increasing number of thought-provoking studies on label-free
116 lymphocytes identification. Light scattering, a parameter commonly used in flow
117 cytometry, is capable of measuring cell size via forward scatter (FSC) and cellular
118 granularity by side scatter (SSC) (Cossarizza et al., 2019). Light scattering has already
119 seen its versatile applications in the screening of lymphocyte samples to distinguish
120 healthy and disease patients such us B-cell chronic lymphocytic leukemia (B-CLL)
121 (Terstappen et al., 1988), cutaneous T-cell lymphoma (Clark et al., 2011) and chronic
122 hepatitises B or C infection (Ruban et al., 2010). The principle underlining light
123 scattering relied disease diagnostics could be that, in general, $CD8^+$ T cells has higher
124 SSC than $CD4^+$ T cells while B cells tend to locate between the resting and activated
125 $CD8^+$ T cells populations (Terstappen et al., 1986a; Terstappen et al., 1986b). Of note,
126 most of the reports have not clearly clarified the potential confounding effects resulting
127 from cell size on SSC pattern given that unhealthy or activated lymphocytes with
128 altered size (higher FSC) are likely to change their SSC profile also (Clark et al., 2011;
129 Loudon et al., 1988; Terstappen et al., 1988). Thus, the question arising is whether
130 SSC distribution is enough to tell the differences of lymphocyte cell types that have
131 indistinguishable cell size, for example, healthy lymphocyte subpopulations under
132 resting status. Moreover, to date, a closer look at the subtle scattering distribution of T

cell differentiation lineages (e.g. naïve/memory T cells) has been neglected. Memory/effector T cells are observed to have more granules than their naïve counterparts under transmission electron microscope (Dimeloe et al., 2016). These findings imply that cell general biophysical attributes (e.g. light scattering) may be further exploited to select for lymphocyte subpopulations with particular functionality, such as for immunotherapy.

Taken together, these inadequacies highlight the need for new methods capable of selecting lymphocyte subpopulations in a label-free manner by relying on general cell biophysical properties. To achieve this, we initially had an in-depth analysis of the light scattering profile (FSC/SSC) of resting human lymphocyte subsets, including NK cells, B cells, total $CD4^+$ T cells, total $CD8^+$ T cells, as well as $CD4^+$ or $CD8^+$ naïve/memory T cell subsets. We found that SSC instead of FSC is a robust biophysical property to distinguish lymphocyte subsets. Generally, lymphocytes with “helper” function such as $CD4^+$ T cells and B cells have a lower SSC than that with “cytotoxic” function such as $CD8^+$ T cells and NK cells. Interestingly, this discrepancy in SSC profile is even more apparent among T cell differentiation lineages regardless of $CD4^+$ or $CD8^+$ T cell type. Younger T cells such as naïve T cells and memory precursors have a significantly lower SSC than their more-differentiated counterparts including central memory T cells, effector memory T cells and terminally effector memory T cells. Inspired by these findings, we developed TRuST, a label-free method for T cell reconstitution using side scatter. TRuST-relied T cell segregation is based on two gating strategies. One is

155 computational gate search aimed to maximize the purity of target cell type of interest.
156 The other is manual gate selection which is easier and more flexible in reconstituting
157 lymphocyte composition instead of focusing on single cell subset. We further
158 demonstrated that reconstituted SSC^{low} cells that are enriched for $CD4^+$ T and naïve T
159 cells have superior expansion capacity and produce more central memory precursors.
160 Finally, using the TRuST-based T cell segregation, we were able to find that both less-
161 differentiated T cell subpopulations and high $CD4^+$ T to $CD8^+$ T ratio in starting cellular
162 material are critical attributes predicting T cell product quality and quantity. This study
163 established TRuST as an effective and reliable technique for label-free lymphocytes
164 selection and reconstitution, which would be useful for lymphocytes biology studies
165 and T cell manufacturing for improved immunotherapy.
166
167 **RESULTS**
168 **TRuST development**
169 TRuST is a label-free approach for lymphocyte subpopulations selection and T cell
170 reconstitution. The development of TRuST was inspired by the intrinsic side-scattering
171 difference of lymphocyte subpopulations including $CD4^+$ T cells, $CD8^+$ T cells, NK cells,
172 B cells, and main T cell differentiation lineages including naïve (T_N, $CD45RA^{high}$
173 $CCR7^{high}$), central memory (T_{CM}, $CD45RA^{dim/-}$ $CCR7^{low}$), effector memory (T_{EM},
174 $CD45RA^{dim/-}$ $CCR7^{-}$) and terminally differentiated effector (T_{EMRA}, $CD45RA^{high}$ $CCR7^{-}$)
175 (**Figures 1A, S1A, and S1B**) (Bohler et al., 2007; Seder and Ahmed, 2003). Due to
176 the heterogeneous SSC patterns of lymphocyte subpopulations, using the pre-stained

lymphocytes for each new sample, it is feasible to find the optimum gate that has the desired purity and yield for target cells of interest via GateID, a computational gate search algorithm for cell type purification (Baron et al., 2019) (**Figure 1B**). Alternatively, a series of manual gates can be set to determine the optimum gate for T cell reconstitution depending on the research aims (**Figure 1C**). The selected gate can be simply adopted and applied for the sorting of unstained lymphocytes (**Figure 1D**). For downstream cell culture assays such as T cell expansion for immunotherapy, the total lymphocytes can be directly sorted into SSC^{low} and SSC^{high} groups that consist of functionally distinct T cell subsets. The sorted cells are subjected to canonical expansion protocol using anti-CD3/CD28 microbeads plus interleukin-2 (IL-2) (**Figures 1D and 1E**). This enables us to study how the initial cell composition affect T cell expansion dynamics, phenotypes formation, and functionality shaping in multifunctional cytokine expression (**Figures 1E and S1C**), and the attributes that contribute to the discrepancies of final T cell products (**Figure 1E**). Together, this work flow demonstrates the utility of TRuST for label-free lymphocyte selection and T cell constitution for downstream lymphocytes biology study.

(main text continued after Figure 1)

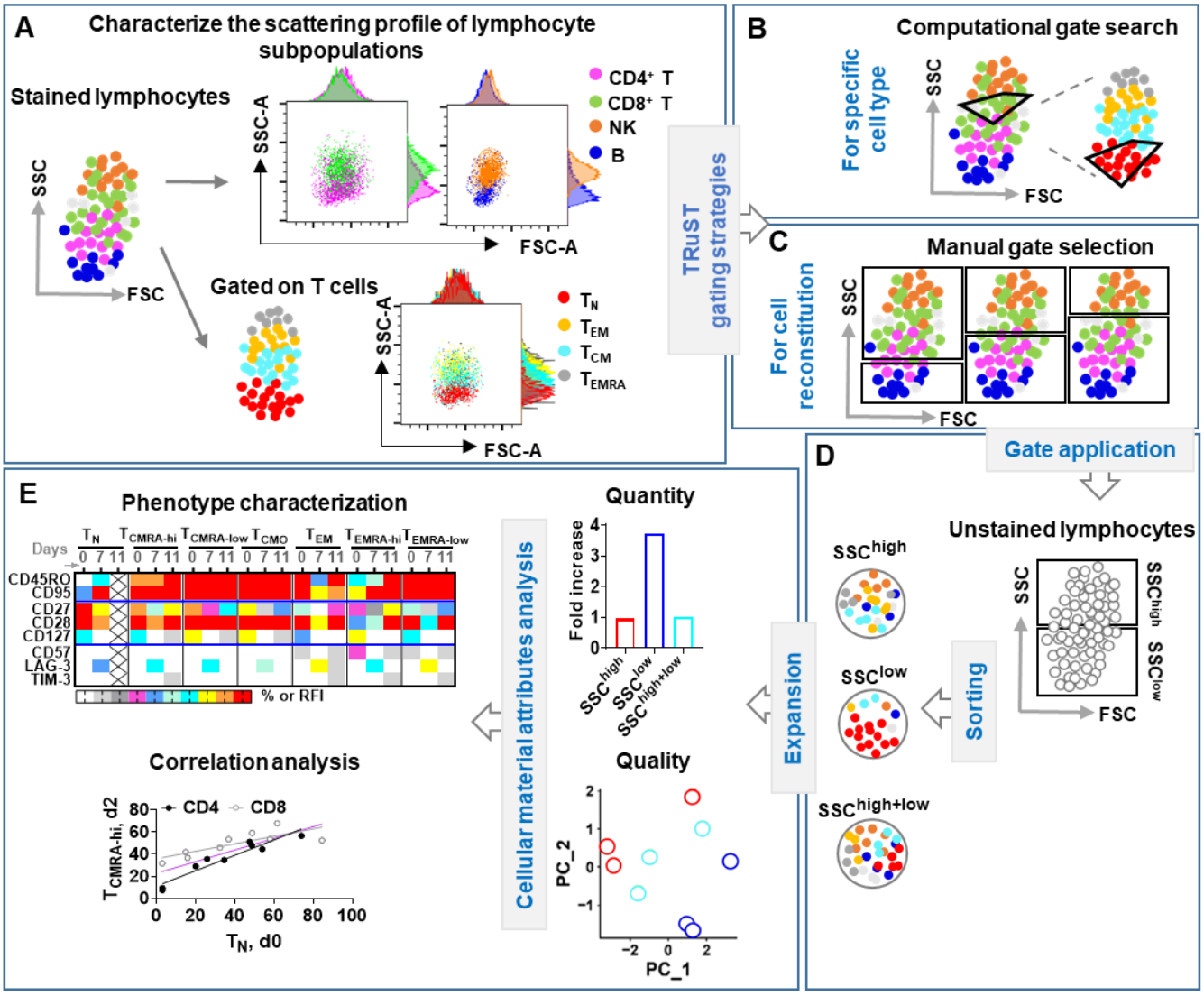

194 **Figure 1. TRuST: An effective approach for label-free T cell selection and reconstitution**

195 (**A**) PBMC samples were stained with lymphocyte subpopulation-representing fluorescence

196 antibodies. Data was acquired by flow cytometer and the forward/side-scattering (FSC/SSC)

197 distribution of main lymphocyte populations and T cell naïve/memory subsets were studied.

198 (**B**) Based on the FSC/SSC profile of lymphocyte populations, a computational gate design

199 algorithm was performed to enrich specific target cell type with optimal purity and yield.

200 (**C**) Alternatively, a manual gating strategy relied on the SSC intensity was used to reconstitute

201 lymphocyte populations with distinct functionality.

(**D**) The manually selected gate was applied for the sorting of unstained lymphocytes for optimum T cell production.

(**E**) A comprehensive comparison of the quantity and quality of T cell products that were derived from cellular materials with different SSC intensity. Characterization of factors contributing to the distinct products by longitudinally phenotypic assessment and correlation analysis.

See also **Table S1** and **Methods**.

TRuST enables effective reconstitution of functionally distinct lymphocyte subpopulations

Lymphocyte cluster can be robustly separated from monocytes and granulocytes based on their FSC/SSC distribution as has been routinely used in flow cytometry. However, a comprehensive study of the subtle scattering profile within various lymphocyte subpopulations is still absent (**Figure 1A**). Using human lymphocytes pre-stained with cell type markers, we found that $CD4^+$ T, B cells and T_N have a lower SSC (low granularity) compared to $CD8^+$ T, NK and differentiated T cells such as T_{CM}, T_{EM} and T_{EMRA} (high granularity) (**Figures 2A and 2B**). With the gradual increase of SSC intensity, there are more $CD8^+$ T and NK cells, as well as more differentiated T cell subsets, leading to percentage reduction of $CD4^+$ T and T_N cells (**Figure S2**). For consistency throughout this work, we manually dived the total lymphocytes into two equal parts (SSC^{high} and SSC^{low}). This gating method is robust enough to either sample staining procedures (**Figures S3A and S3B**) or voltages change applied during flow cytometry data acquiring (**Figures S3A, S3C, and S3D**). On the contrary, FSC can

only differentiate B cells from NK cells (**Figures S3E-S3G**). The nearly unaltered light scattering profiles between stained and unstained cells (**Figure S3B**) enable us to directly apply the gate in sorting of unstained lymphocytes (**Figure 2C**). Similarly, sorted SSC^{low} group enriches for $CD4^+$ T cells and naïve T cells while SSC^{high} cluster enriches for $CD8^+$ T, NK and other more-differentiated T cell counterparts including T_{CM}, T_{EM} and T_{EMRA} (**Figures 2D-2G**). Deep-ultraviolet light (UV) has been adopted for label-free molecular imaging (Zeskind et al., 2007) and hematology analysis (Ojaghi et al., 2020) thanks to its shorter wavelength. Thus, it is interesting to study whether UV light (e.g. UV405 nm) can be used to further improve the scattering resolution of cell morphometric structure under blue light (e.g. B488 nm). However, we observed that a double side-scatter (UV405/B488) based sorting strategy (**Figure S3H**) did not improve the general segregation efficiency of CD4/CD8 T cells, NK/B cells and naïve/memory T cells as well (**Figures S3I-S3M**). Therefore, global cellular granularity, as represented by SSC intensity, could be a general biophysical property used for the separation of lymphocyte subpopulations.

Next, we sought to characterize the phenotypes of sorted cell populations based solely on SSC intensity. The sorted SSC^{low} cells displayed a higher expression of costimulatory receptors such as CD27 and CD28 but a lower expression of differentiation marker CD127, memory marker CD45RO and activation/inhibition factors CD95/CD57 (**Figure 2H**), consistent with a larger number of naïve T cells in this cell cluster. Unexpectedly, T cells of the same differentiation lineage but different

SSC intensity also manifested some distinguishable phenotypic traits (**Figures 2I and 2J**). For example, either T_N or T_{CM} in SSC^{low} group had reduced CD127, CD95 and to a less extent CD57 (**Figure 2I**). Instead, T_{CM} of SSC^{low} cluster had increased CD27 (**Figure 2I**) and CCR7/CD45RA abundance (**Figure 2J**), suggesting its central memory precursor-like phenotype. Functionally, in response to short pulse of protein kinase C (PKC) stimulus, the SSC^{low} lymphocytes produced a large amount of IL-2 but reduced IFN-γ-involved immediate effector cytokines (**Figures 2K and 2L**), resembling cytokine expression dynamics of early-differentiated T cells (Denton et al., 2011; Hinrichs et al., 2009). The large amount of IFN-γ but near absence of IL-2 expression in non-T lymphocytes of SSC^{high} group is in line with a high proportion of NK cells in this cluster (**Figures 2M and 2E**). Taken together, these findings suggest that younger T cell lineages including naïve T cells and central memory precursors are intrinsically endowed with a lower SSC, which, concurrently with a higher ratio of $CD4^+$ T to $CD8^+$ T cells can be effectively enriched by TRuST.

(main text continued after Figure 2)

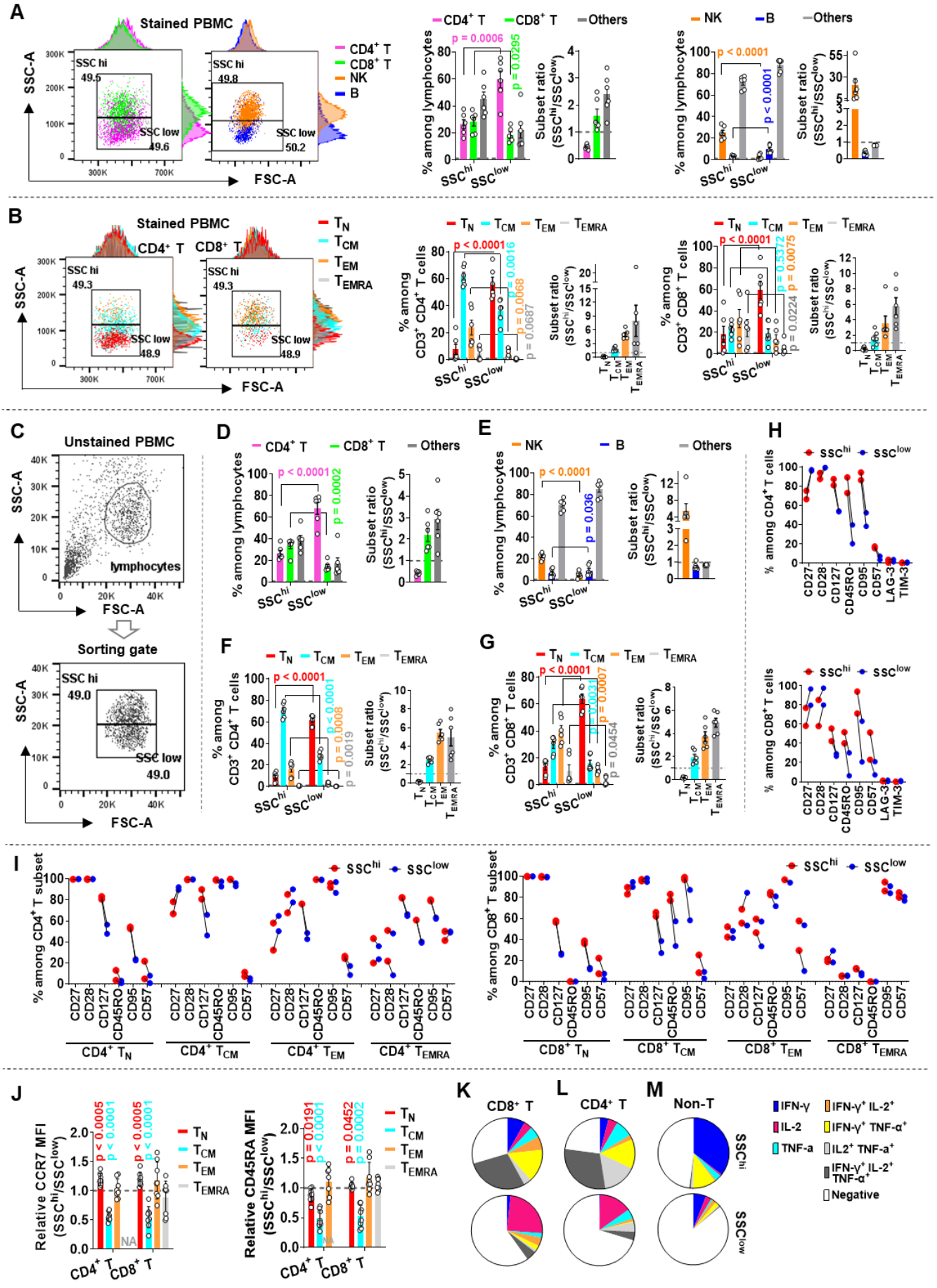

Figure 2. SSC is a robust biophysical property for TRuST development

(**A and B**) PBMC samples were stained with surface marker antibodies before flow cytometry data acquiring. Dot plots are representative FSC/SSC profiles of $CD3^+$ $CD4^+$ T/$CD3^+$ $CD8^+$ T cells (**A, left dot plot**), NK/B cells (**A, right dot plot**), and T_N/T_{CM}/T_{EM}/T_{EMRA} cell subsets (**B**). For statistical analysis, samples were gated to equally divide the cells into two clusters based on the cluster of total lymphocytes (not shown in the dot plots) (**A and B, dot plots**) and the percentage of $CD3^+$ $CD4^+$ T/$CD3^+$ $CD8^+$ T cells, NK/B cells, and T_N/T_{CM}/T_{EM}/T_{EMRA} cell subsets within SSC^{hi} or SSC^{low} cluster were summarized (**A and B, histograms**). Two independent experiments for each donor (n = 3) were compiled. A two-tailed, paired *t*-test between the two groups was performed. Error bars indicate mean ± SEM.

(**C-G**) Unstained PBMC samples were equally sorted into SSC^{hi} and SSC^{low} populations before lymphocyte subtypes determination (**C**). Characterization of the percentage of $CD3^+$ $CD4^+$ T/$CD3^+$ $CD8^+$ T cells **(D)**, NK/B cells (**E**), and T_N/T_{CM}/T_{EM}/T_{EMRA} (**F and G**) among the sorted SSC^{hi} and SSC^{low} cell populations. Data from three donor samples with two independent experiments for each donor were compiled. A two-tailed, paired *t*-test between the two groups was performed. Error bars indicate mean ± SEM.

(H and I) A comparison of the expression profiles of selected phenotyping markers in sorted SSC^{hi} and SSC^{low} cells (**H**), and characterization of the phenotypic traits of the same naïve/memory T subset derived from SSC^{hi} or SSC^{low} cell clusters (**I**). Each dot represents data of one donor PBMC (**H and I**).

(J) The relative expression level of CCR7 and CD45RA in $CD4^+$ T or $CD8^+$ T naïve/memory subsets from sorted SSC^{hi} and SSC^{low} cells. Plots represent data from three donor PBMC. Cell

subset nearly undetectable is indicated as "NA". A two-tailed, unpaired *t*-test between SSC^{hi} and SSC^{low} groups was performed. Error bars indicate mean ± SEM.

(**K-M**) Sorted SSC^{hi} and SSC^{low} cells were stimulated with PMA plus ionomycin for 4 hours before intracellular staining. Shown are the multifunctional cytokine expression profile of $CD3^+$ $CD8^+$ T cells (**K**), $CD3^+$ $CD8^-$ T cells (**L**), and $CD3^-$ cells (**M**) within sorted sorted SSC^{hi} or SSC^{low} cells (n = 2).

See also **Figure S1** for gating methods in determining cell types and multifunctionality analysis, **Figures S2** and **S3** for manual gating selection.

TRuST enhances lymphocyte subset selection using computational gate design

While manual gating for cell sorting is a simple and effective way to reconstitute lymphocytes, it could be less efficient for the selection of specific lymphocyte subset. Thus, we took advantage of the recently developed computational algorithm, GateID (Baron et al., 2019), that relies on the general properties (e.g. cell size, granularity and mitochondrial content) to search for the optimum gate for cell type enrichment. Using this method, it is possible to obtain lymphocyte subsets of interest with desired purity and yield (**Figure 3**).

Naïve T cells can be obtained with the highest purity and acceptable yield (**Figure 3E**), in line with their location within the cell group of lowest SSC (**Figure 2B**). T_{CM}, T_{EM}, T_{EMRA}, total $CD4^+$ T and NK cells can also be significantly enriched, but at the expense of quickly dropped yields (**Figures 3F-3H, 3A, and 3C**). On the other hand, $CD8^+$ T

306 cells and B cells tend to be the most difficult lymphocytes to be enriched with an
307 improved purify and appreciable yield, partially due to their relatively homogeneous
308 side-scattering distribution diffused into other lymphocytes (**Figures 3B and 3D**).
309 Notably, given that a comparable FSC/SSC pattern was observed between unstained
310 and stained cell samples (**Figure S3B**), it would be possible to directly apply the
311 predicted gate in actual sorting experiments without gate normalization. Thus,
312 combining TRuST with computational gate search, it is feasible to improve the purity
313 of lymphocyte subsets with a reduced yet still acceptable recovery rate.

314 (main text continued after Figure 3)

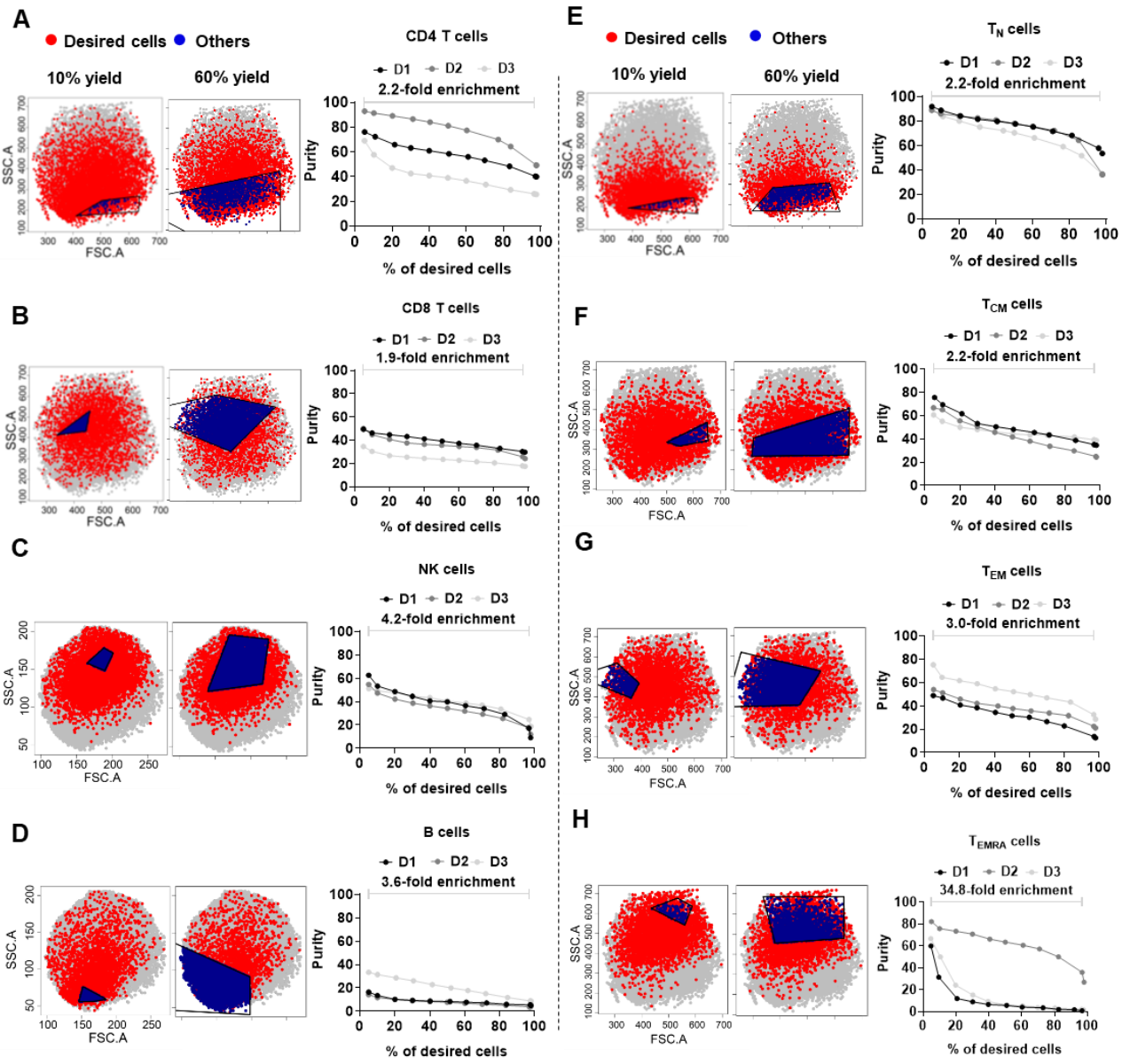

315 **Figure 3. TRuST enhances enrichment of specific lymphocyte subset using**

316 **computational gate design**

317 (**A-H**) The raw readouts corresponding to FSC and SSC parameters for each cell type as shown

318 in Figures 2A and 2B were exported, named and reanalyzed by GateID algorithm to select the

319 desired cell type. The enrichment efficiency of $CD3^+$ $CD4^+$ T (**A**), $CD3^+$ $CD8^+$ T (**B**), NK (**C**) and

320 B cells (**D**), or selection of total T_N (**E**), T_{CM} (**F**), T_{EM} (**G**) and T_{EMRA} subsets (**H**) were plotted by

321 automatically adjustable gating threshold. For each cell type/subset, two representative gating

322 plots corresponding to 10% and 60% yields of desired cells, and the correlation plots between

purity and yield are shown. An average enrichment fold-increase between ~100% yield to ~5% yield (n = 3) is indicated. The percentage of desired cells (yield) is calculated as the number of desired cells within the gating to that of total desired cells among the whole cell population. The purity indicates the proportion of desired cells to that of total cell numbers within each gate. See also **Methods**.

TRuST-relied lymphocytes reconstitution improves T cell product quantity and quality

When practical feasibility and manufacturing cost are taken into consideration, such as T cell production for adoptive immunotherapy, it might not be necessary to enrich for a very specific cell type at the expense of greatly reduced cell recovery. Instead, strategies that enable the reconstitution of lymphocyte subpopulations to maximally improve cell production without compromising yield and quality would be preferable.

Given that T cell product derived from less-differentiated T cells show better outcome in adoptive immunotherapy (Berger et al., 2008; Finney et al., 2019; Fraietta et al., 2018; Hinrichs et al., 2011), we next investigated how compositional difference of starting T cell materials reconstituted solely by TRuST under manual gate selection (**Figure 2C**) may affect the diversity of final T cell products. In response to anti-CD3/CD28 microbeads stimulation, an antigen-presenting cells-mimic activation approach widely used for T cell manufacturing, SSC^{low} cells consisting of T_N and younger T_{CM} cells were endowed with superior proliferation capacity, and achieved an

345 average increase of total nucleated cells (TNC) by 2.3-fold at day 7 and 3.2-fold at day
346 11 with 3-fold increase for $CD4^+$ T and 4-fold increase for $CD8^+$ T subtypes (**Figures**
347 **4A-4C and S4A-S4C**). Unexpectedly, the expansion potential of the $SSC^{high+low}$ group
348 appeared to be equivalent to that of SSC^{high} population (**Figures 4A-4C**), likely due to
349 the precocious differentiation of naïve cells driven by existing effector/memory cells
350 (Klebanoff et al., 2016) and the inhibitory effects caused by large amount of NK cells
351 (Cook and Whitmire, 2013).
352
353 Yellow fever-specific central memory $CD8^+$ T cells with high CD45RA expression was
354 demonstrated to be a critical cell subpopulation accounting for persistent immune
355 memory, which resembled stem cell-like memory subset ($CCR7^+$ $CD45RA^+$ $CD58^+$
356 $CD95^+$ $CD28^+$ $CD27^+$ T_{SCM}) (Fuertes Marraco et al., 2015). Thus, based on the dynamic
357 change of CCR7/CD45RA expression, an in-depth gating strategy was used to classify
358 T cell subsets into T_N, naïve population-closest $CD45RA^{high}$ T_{CM} ($T_{CMRA\text{-}hi}$), $CD45RA^{low}$
359 T_{CM} ($T_{CMRA\text{-}low}$), $CD45RA^{negative}$ T_{CM} (T_{CMO}), and T_{EM} with CD45RA expression as
360 $CD45RA^{high}$ T_{EM} ($T_{EMRA\text{-}hi}$), $CD45RA^{low}$ T_{EM} ($T_{EMRA\text{-}low}$) and $CD45RA^{negative}$ T_{EM} (T_{EM})
361 (**Figure S4D**). Longitudinal assessment of T cell naïve/memory composition during
362 expansion showed that, compared to SSC^{high} descendants, SSC^{low} cells-derived
363 progenies generally had a higher portion of $T_{CMRA\text{-}hi}$ but less $T_{CMRA\text{-}low}$ and other more-
364 differentiated cell subsets (e.g. T_{CMO} and $T_{EMRA\text{-}low}$) (**Figures 4D, 4E, and S4E-S4H**).
365 This finding is consistent with a continuously higher expression of co-stimulatory
366 molecules CD27/CD28 that favor cell survival and proliferation (**Figures 4F, S5A, and**

S5B) while other phenotypic traits like memory marker CD45RO and inhibition/senescence receptors such as CD57, LAG-3 and TIM-3 were more dynamically variable (**Figures S5A and S5B**).

Functionally, the SSC^{low} cells-derived products responded faster to short period of PKC activation by producing more IL-2 and TNF-α but less IFN-γ (**Figure 4G**). SSC^{low} cells-derived $CD4^+$ T cells displayed better compliance with this tendency by expressing the highest amount of early-effector cytokines (e.g. IL-2^+ and IL-2^+ TNF-α^+) and less late-effector cytokines (e.g. IFN-γ^+, IFN-γ^+ IL-2^+ and IFN-γ^+ TNF-α^+) (**Figure 4H**). The $CD8^+$ T counterpart shows a higher diversity and even conflicts these observations post extensive expansion (e.g. donor 3 at day 11) (**Figure 4I**). Nevertheless, the global cytokine-expressing trait of cell products generated from SSC^{low} group is more naïve-like (**Figures S5C and S5D**) (Gattinoni et al., 2005; Hinrichs et al., 2009), indicating a synergic functionality may happen when $CD4^+$ T and $CD8^+$ T co-exist in culture system. Superior engraftment and persistence of infused T cells are critical parameters for improved therapeutic index. Extensively expanded T cells from either SSC^{high}, SSC^{low} or reconstituted $SSC^{high+low}$ group had similar chemotactic migration to CCL19/CCL21 (**Figure 4J**), in line with their comparable proportion of total T_{CM} (**Figures 4D and 4E**). However, in response to multiple stimulation by CD3/CD28 engagement, the SSC^{low}-derived progenies were endowed with greater capability for multiple expansion under both IL-2 and homeostatic cytokines IL-7/IL-15 (**Figure 4K**), presumably associated with a higher expression of costimulatory markers CD27/CD28 (**Figures 4F, S5A, and**

389 **S5B**) and underlined epidemic modification favoring cell persistence.

390

391 Overall, the SSC^{low} lymphocytes-derived T cell product is discernable from that of

392 SSC^{high} group, the former manifests not only superior proliferation but also earlier

393 phenotypes characteristic of apparently increased $T_{CMRA\text{-}hi}$ and enhanced IL-2/TNF-α

394 expression for both $CD4^+$ T and $CD8^+$ T cells ((**Figures 4L and 4M**).

395 (main text continued after Figure 4)

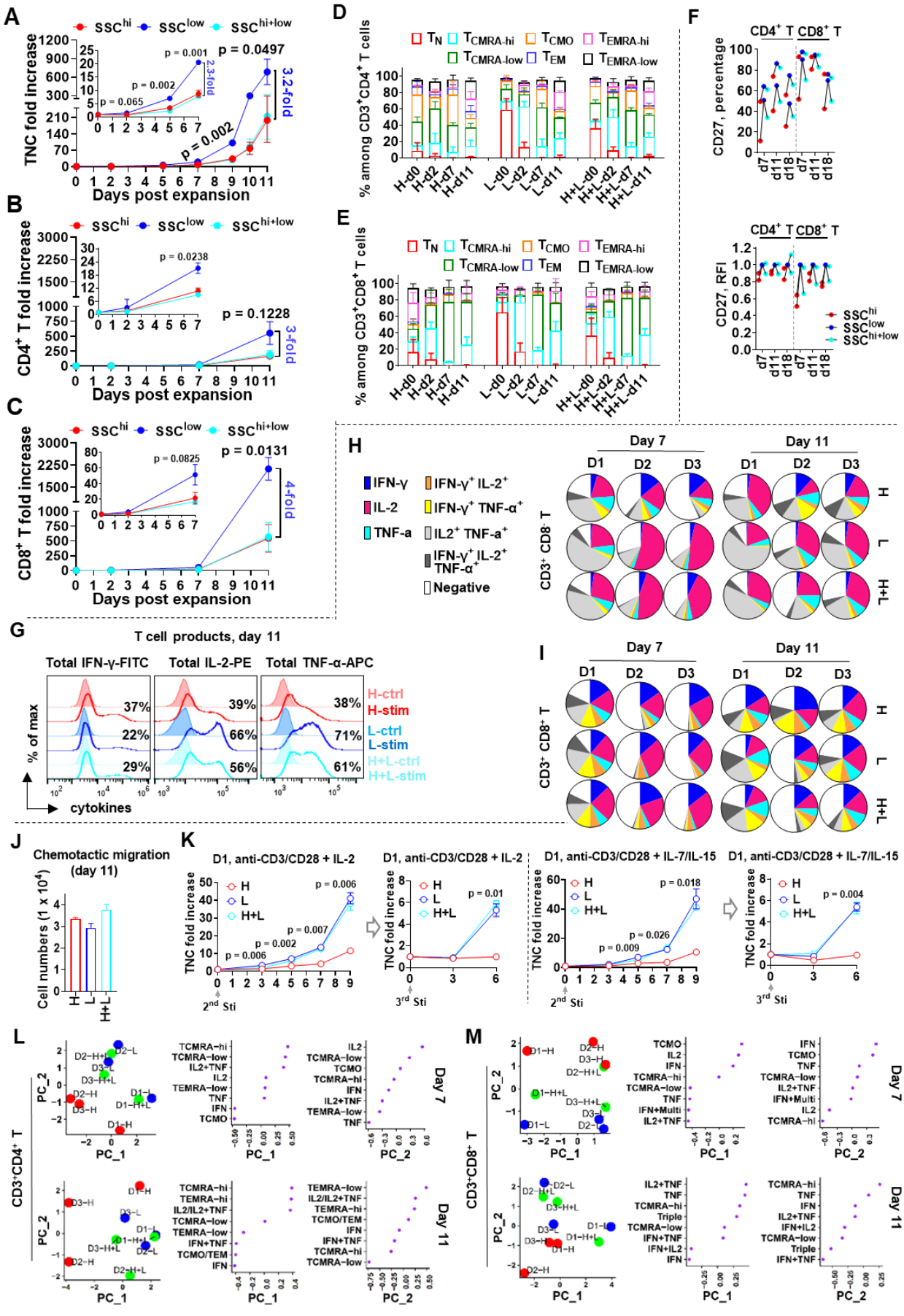

Figure 4. TRuST-relied lymphocytes reconstitution improves T cell product quantity and quality

(**A-C**) Expansion efficiency of lymphocytes derived from SSC^{hi}, SSC^{low}, or reconstituted SSC^{hi+low} cells at a ratio of 1:1 are represented by TNC fold increase (**A**), $CD3^+$ $CD4^+$ T (**B**) and $CD3^+$ $CD8^+$ T fold increase (**C**). Data are presented as means ± S.E.M (n = 3). Paired two-tailed *t*-test between SSC^{low} and SSC^{hi} group was performed. Error bars indicate mean ± SEM.

(**D and E**) Compositional change of naive/memory subsets in $CD3^+$ $CD4^+$ T (**D**) or $CD3^+$ $CD8^+$ T cells (**E**) plotted along the days of expansion. Error bars indicate mean ± SEM.

(**F**) Percentage and relative fluorescence intensity (RFI) of CD27.

(**G-I**) Representative histogram plot of IFN-γ/IL-2/TNF-α expression of cell product at day 11 post expansion derived from cell groups with different side-scattering intensity (**G**). Multifunctional cytokine expression of total $CD4^+$ T (**H**) or $CD8^+$ T (**I**) cells at day 7 and day 11 post expansion (n = 3) with 2 independent experiments for donor 1 and 2.

(**J**) Migration capacity of T cells at day 11 post expansion derived from SSC^{hi}, SSC^{low} and SSC^{hi+low} groups. Error bars indicate mean ± SEM.

(**K**) Responsiveness of effector cells descended from SSC^{hi}, SSC^{low} and SSC^{hi+low} groups at day 11 post expansion to multi-stimulation by CD3/CD28 engagement with IL-2 (**top**) or homeostatic cytokines IL-7 plus IL-15 (**bottom**). Duplicates for each sample were performed. Unpaired two-tailed *t*-test between SSC^{low} and SSC^{hi} group was performed. Error bars indicate mean ± SEM.

(**L and M**) All phenotypic parameters and cytokine-expressing values were integrated together for PCA calculation. For data from day 7, $IFN\text{-}\gamma^+$ $IL\text{-}2^+$/ $IFN\text{-}\gamma^+$ $TNF\text{-}\alpha^+$/ $IFN\text{-}\gamma^+$ $IL\text{-}2^+$ $TNF\text{-}\alpha^+$ were

419 combined as “IFN+Multi”. “H” and “L” indicate “SSC^{hi}” and “SSC^{low}”, respectively.

420 See also **Figures S4A-4C and S4E-4G** for individual data, and **Figure S4D** for gating method

421 in cell differential lineages characterization.

422

423 **Increased $T_{CMRA\text{-}hi}$ derived from the SSC^{low} cell cluster resembles central memory**

424 **precursors**

425 Given the significant accumulation of $T_{CMRA\text{-}hi}$ subpopulation that falls in the

426 conventional central memory gate of the cell products derived from SSC^{low} group

427 (**Figures S4D and S1B**), we next sought to define the natural characteristics of this T

428 cell subset by longitudinally determining its phenotypic change during expansion

429 (**Figures 5A-5E**). We showed that $T_{CMRA\text{-}hi}$ had a higher expression of canonical

430 memory marker CD45RO than T_N but lower than $T_{CMRA\text{-}low}$ and T_{CMO} regardless of $CD3^+$

431 $CD4^+$ T cells (**Figures 5B and 5C**) or $CD3^+$ $CD8^+$ T cells (**Figures 5D and 5E**). While

432 all resting central memory T subsets ($T_{CMRA\text{-}hi}$, $T_{CMRA\text{-}low}$ and T_{CMO} at day 0) presented

433 higher death receptor CD95 (a marker used to distinguish T_{SCM} from T_N) (Fuertes

434 Marraco et al., 2015; Gattinoni et al., 2011) than the T_N subset, they became similar

435 post activation with nearly complete expression of this marker (**Figures 5B-5E**).

436 Notably, the expression of co-stimulatory markers such as CD27 and CD28 was more

437 comparable between $T_{CMRA\text{-}hi}$ and T_N, especially for $CD8^+$ T cells (**Figures 5D and 5E**).

438 With regard to inhibitory or senescent factors (e.g. CD57, LAG-3 and TIM-3), $CD8^+$

439 $T_{CMRA\text{-}hi}$ and $CD8^+$ T_N expressed similar but less CD57 than other $CD8^+$ T subsets

440 before activation, which however decayed to a dim expression in all subsets post

441 extensive proliferation (**Figure 5D**). In addition, LAG-3 was dramatically increased in
442 activated $CD8^+$ T subsets at day 7 and decreased at day 11, during which $T_{CMRA\text{-}hi}$
443 tended to have a higher LAG-3 expression compared to T_N but still comparable or even
444 lower than other memory subsets (**Figures 5D and 5E**). These findings suggest that
445 $T_{CMRA\text{-}hi}$ is phenotypically distinct from T_N and resembles the central memory precursor
446 with naïve-like phenotypic traits ($CCR7^+$ $CD45RA^{high}$ $CD95^+$ $CD28^+$ $CD27^+$), which
447 could be taken into consideration in the evaluation of T cell products by different
448 manufacturing protocols.
449
450 The burst increase of $T_{CMRA\text{-}hi}$ at the beginning of T cell activation (day 2, **Figures 4D**
451 **and 4E**) is well correlated with the initial proportion of T_N, and this trend maintains from
452 day 7 to day 11 (**Figure 5F**). In contrast, the existence of more-differentiated $CD4^+$
453 T_{CMO} (**Figure 5G**) and $CD4^+$ $T_{CMRA\text{-}low}$ (**Figure 5H**) in starting cell materials tend to
454 counteract the generation of $CD4^+$ $T_{CMRA\text{-}hi}$ despite the effects being varied at different
455 stages post activation. Also, a high number of $CD8^+$ $T_{CMRA\text{-}low}$ (**Figure 5H**) and $CD8^+$
456 T_{EMRA} (**Figure 5I**) are more likely to reduce the production of $CD8^+$ $T_{CMRA\text{-}hi}$. However, it
457 is less predictable for $CD8^+$ $T_{EMRA\text{-}hi}$ generation based on the cell composition before
458 expansion (**Figures S6D-S6G**). Of note, $CD4^+$ T_N and $CD4^+$ T_{CMO} (**Figures S6D and**
459 **S6E**) do show evidences of contrary correlation with $CD4^+$ $T_{EMRA\text{-}hi}$ production. There
460 was a sharp decrease of $CD8^+$ $T_{EMRA\text{-}hi}$ cells post activation in the SSC^{high} group that
461 consists of a larger proportion of differentiated cell subpopulations (**Figures S4E and**
462 **S4F**). Thus the dynamical accumulation of terminally differentiated $T_{EMRA\text{-}hi}$ cells from

463 SSC^{low} groups (**Figures S4F and S4G**) could be partially attributed to a more survival-
464 favoring environment enriched in less-differentiated cell subsets (e.g. T_N). Additionally,
465 $T_{EMRA\text{-}hi}$ displays higher CD27/CD28 expression than the CD45RA-reduced $T_{EMRA\text{-}low}$ or
466 T_{EM} subset, which is especially apparent for $CD8^+$ T cells during expansion (**Figures**
467 **5D and 5E**), suggesting functional potency of this cell subset in cell therapy when
468 alternative co-stimulatory signaling (e.g. CD28 and 4-1-BB) and accessory factors for
469 end-stage effector cells proliferation are involved (Fuertes Marraco et al., 2015; van
470 Leeuwen et al., 2002; Waller et al., 2007). Taken together, these results show that the
471 pre-enrichment of less-differentiated cells simply by side scatter enables the
472 maintenance of naïve-like central memory precursors ($T_{CMRA\text{-}hi}$) and accordingly
473 contributes to the slight accumulation of terminally effector-like T_{EM} ($T_{EMRA\text{-}hi}$).

474 (main text continued after Figure 5)

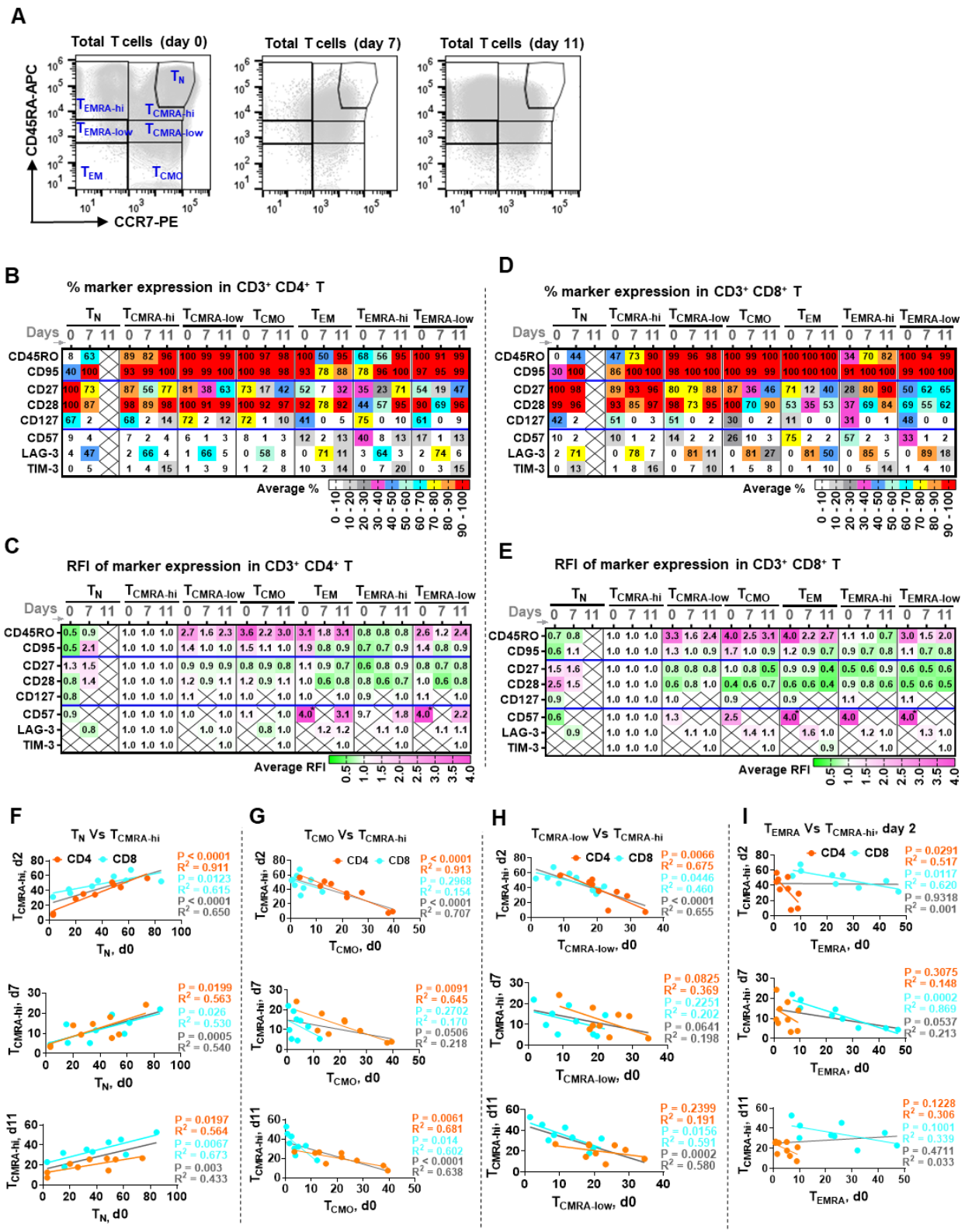

475 **Figure 5. Increased $T_{CMRA\text{-}hi}$ derived from SSC^{low} cell cluster resembles central memory**

476 **precursor**

477 (**A**) Representative plots show the superimposed total T cell populations derived from SSC^{hi},

478 SSC^{low} and SSC^{hi+low} cells at day 0, 7, 11. T cell subsets to be analyzed are gated.

479 (**B-E**) Longitudinal assessment of phenotypic change of $T_{CMRA-hi}$ compared to other T cell
480 subsets. Average expression frequency of the indicated markers within $CD4^+$ T or $CD8^+$ T
481 subsets (**B and E**) and abundance as presented by relative fluorescence intensity (RFI) was
482 reported after normalization to the values of $T_{CMRA-hi}$ for each marker of the same time points
483 respectively (**C and E**). The numbers highlighted by "*" indicate values large than 4. The cross
484 indicates omitted data due to low cell percentages for marker expression identification or
485 insufficient counts for MFI calculation.

486 (**F-I**) Correlation analysis of starting effector/memory composition, including T_N (**F**), T_{CMO} (**G**),
487 $T_{CMRA-low}$ (**H**), and total T_{EMRA} (**I**), with the percentage of generated $T_{CMRA-hi}$ among cell products
488 of each time point. Data from the same day from all of the three donors were combined. Each
489 dot represents the percentage of generated $T_{CMRA-hi}$ versus the initial cellular component of its
490 starting cell material (day 0). The solid black line indicates combined linear regression using all
491 the dots in that plot (**F-I**).

492 See also **Figure S4D** for gating method in identifying the dynamic change of T cell lineages
493 during expansion, and **Figures S6A-6C** for individual data of phenotypic marker expression in
494 each T cell subset. **Figures S6D-6G** for correlation analysis of initial cell composition with $T_{EMRA-hi}$
495 generation.

496

497 **$CD4^+$ T cells help is critical for optimum $CD8^+$ T cells proliferation**

498 A shaper ratio decrease of CD4/CD8 T cells during expansion was observed for cells
499 from lower side-scatter, which initially have the largest proportion of $CD4^+$ T cells and

later the highest expansion capacity (**Figure 6A**). This has inspired us to understand the role of $CD4^+$ T-$CD8^+$ T cells crosstalk in T cell proliferation and functionality shaping despite the absence of specific external antigens (**Figure 6B**).

Co-culture of $CD4^+$ T-$CD8^+$ T cells favored the global expansion of total T cells (**Figure 6C**). Help from $CD4^+$ T cells was required for $CD8^+$ T cells maximal proliferation by an average of 6-fold increase at day 7 and 8.5-fold increase at 18 (**Figure 6D**). In turn, $CD8^+$ T cells reduced $CD4^+$ T cells expansion to a lesser extent by 1.4-fold reduction at day 7 and 2-fold decrease at day 11 and 18 (**Figure 6E**). Thus, the orchestrated growth dynamics within $CD4^+$ T and $CD8^+$ T cells results in final T cell products with not only different absolute cell numbers (**Figure 6C**) but also discernable $CD4^+$ T to $CD8^+$ T ratio (**Figure 6F**).

(main text continued after Figure 6)

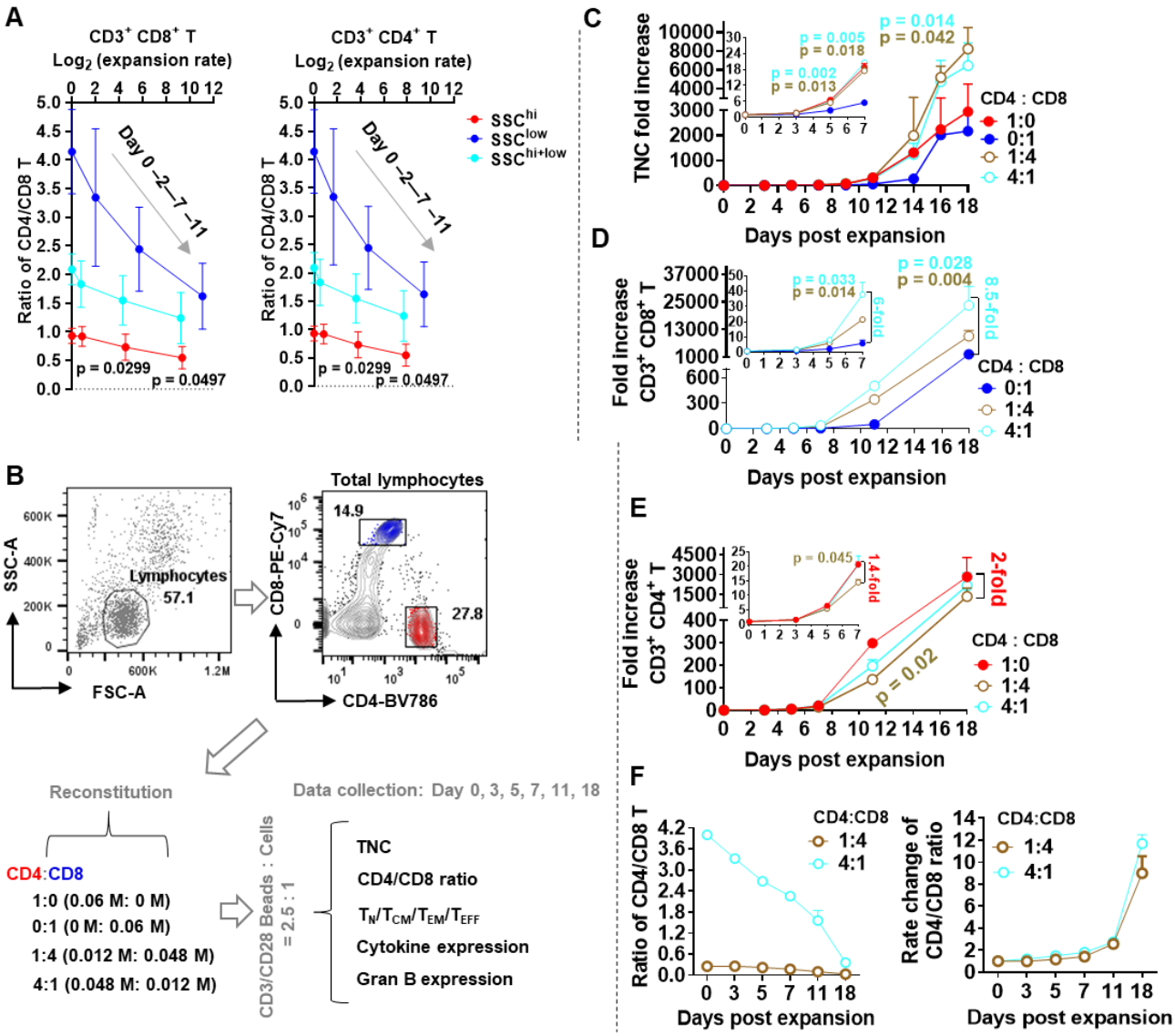

513 **Figure 6. CD4⁺ T help is required for optimal CD8⁺ T expansion**

514 (**A**) Synchronized T cell expansion efficiency with the ratio change of CD4/CD8 T cells starting

515 from cell materials of different side-scattering intensity. Data are representative of three donors

516 as described in Figures 4A-4C. Graphs represent means ± S.E.M (n = 3). Paired two-tailed *t*-

517 test was used for statistical calculation between SSC^{hi} and SSC^{low} group. Error bars indicate

518 mean ± SEM.

519 (**B**) $CD4^+$ cells and $CD8^+$ cells were sorted and validated to have more than 96% of $CD3^+$ $CD4^+$

520 T and $CD3^+$ $CD8^+$ T cells, respectively. $CD4^+$ cells and $CD8^+$ cells were reconstituted at the

indicated ratio and co-expanded by CD3/CD28 engagement.

(**C-E**) Proliferative potential of TNC (**C**), $CD3^+$ $CD4^+$ T (**D**) or $CD3^+$ $CD8^+$ T cells (**E**) in condition of CD4-CD8 T cells co-culture. Data of day 5, 7, 11 and 18 represent two independent experiments. Unpaired two-tailed *t*-test compared to culture condition of $CD8^+$ T cells only (**C and D**) or $CD4^+$ T cells only (**E**). Error bars indicate mean ± SEM.

(**F**) Changes in the ratios of $CD4^+$ T to $CD8^+$ T cells in samples starting with high (4:1) and low (1:4) ratios of CD4 to CD8 T cells. Error bars indicate mean ± SEM.

$CD4^+$ T cells promote $CD8^+$ T early central memory pool maintenance

By longitudinal assessment of T cell naive/memory composition, we found that optimum maintenance of $CD8^+$ $T_{CMRA\text{-}hi}$ but less $CD8^+$ T_{EM} and $CD8^+$ $T_{EMRA\text{-}low}$ can be achieved in the presence of $CD4^+$ T cells in a ratio-dependent manner (**Figure 7A**). Interestingly, the mild accumulation of $CD8^+$ $T_{EMRA\text{-}hi}$ was also observed, similar to that of SSC^{low} cells-derived descendants (**Figures S4F and S4G**), indicating a superior culture environment for T cell survival endowed by $CD4^+$ T. On the contrary, a large proportion of $CD8^+$ T cells tended to counteract $CD4^+$ $T_{CMRA\text{-}hi}$ generation during the early expansion stages (e.g. day 0-7) (**Figure 7B**). This is reflected by a higher expression of CD28 on $CD8^+$ T cells but lower on $CD4^+$ T cells throughout the co-culture course (**Figures 7C**, **S7A, and S7B**). Also, the increased number of less-differentiated $CD8^+$ T cells generated at day 11 under $CD4^+$ T-$CD8^+$ T co-expansion is consistent with a greater migration ability to CCL19/CCL21 (**Figure 7D**).

With respect to functional shaping, it is clear that $CD4^+$ T and $CD8^+$ T cells mutually endowed each other with a higher granzyme B expression during the initial proliferation phase (day 0 - 7, **Figures 7E and 7F**). However, $CD8^+$ T cells from all conditional groups became comparable in granzyme B expression at day 11 while a larger portion of $CD4^+$ T cells continued to express granzyme B in the presence of $CD8^+$ T cells (**Figures 7F**). In addition, $CD4^+$ T help contributed to the generation of less-differentiated $CD8^+$ T cells characteristic of enhanced IL-2 /TNF-α but reduced IFN-γ production (**Figures 7G**). Instead, $CD8^+$ T cells showed only moderate inhibition on the secretion of IL-2/TNF-α by $CD4^+$ T cells (**Figures 7G**). Moreover, the inclusion of resting $CD4^+$ T cells was able to rescue the expansion potency of extensively differentiated $CD8^+$ T cells (**Figures 7H**). Therefore, despite the absence of cognate antigens, help from $CD4^+$ T cells is critical for shaping the proliferative capacity and functional potency of $CD8^+$ T cells, which should be an important factor to be considered during T cell manufacturing.

(main text continued after Figure 7)

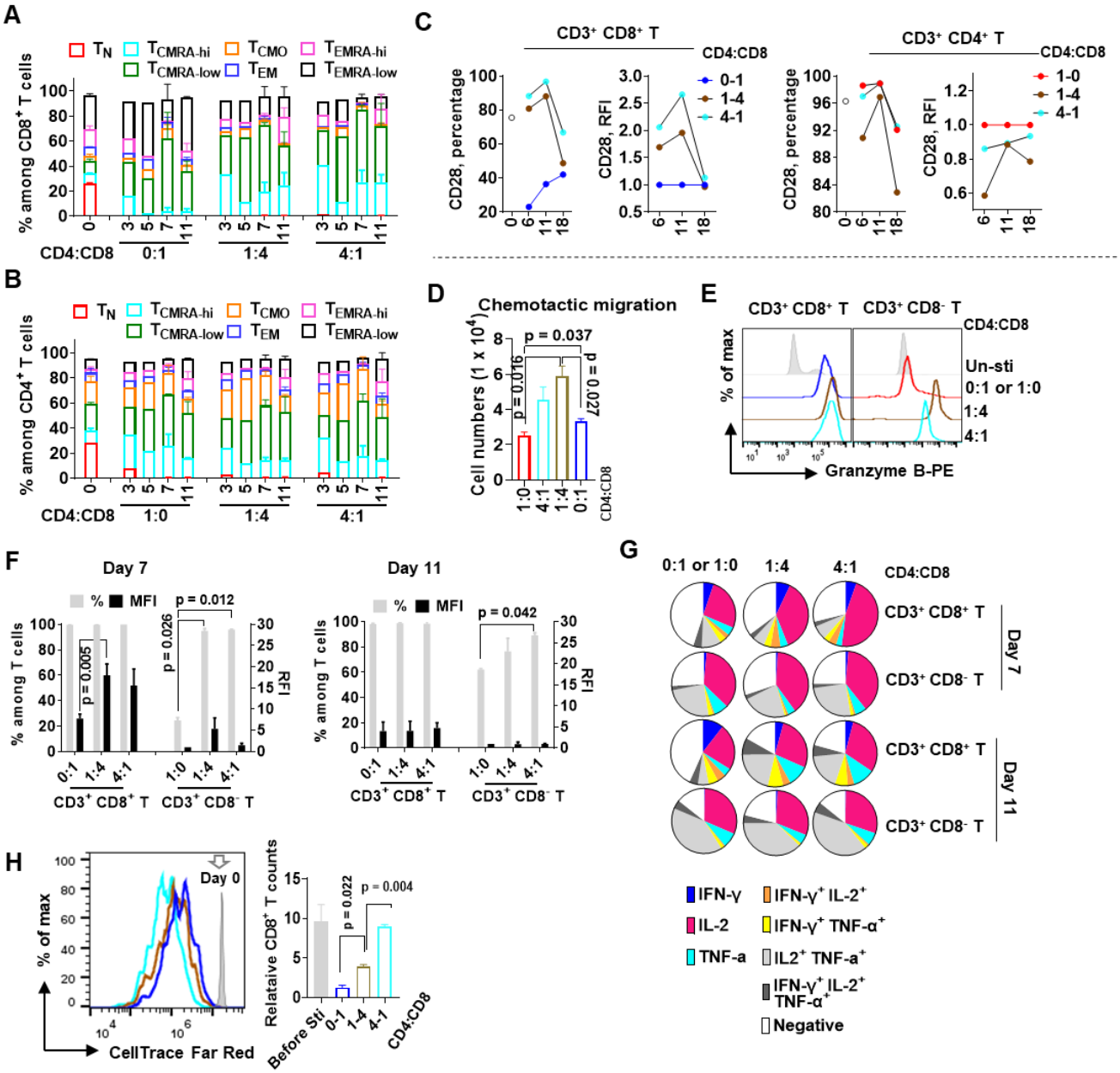

Figure 7. CD4⁺ T cells promote the maintenance of CD8⁺ T early central memory pool

(**A and B**) Compositional change of naive/memory subsets in CD3⁺ CD8⁺ T (**A**) or CD3⁺ CD4⁺ T cells (**B**) along the days of expansion. Data for day 0, 7 and 11 are representative of two independent experiments. Error bars indicate mean ± SEM.

(**C**) Dynamic expression of CD28 is represented by both percentage and relative fluorescence intensity of T cell products from CD4-CD8 T cells co-expansion. The medium fluorescence intensity (MFI) is normalized to that of CD4⁺ T cells or CD8⁺ T cells cultured separately at the

indicated time points.

(D) CCL21/CCL19-driven migration capacity of T cell generated at day 11 starting from different $CD4^+$ to $CD8^+$ T cell ratio. Data represents duplicate experiments. Error bars indicate mean ± SEM.

(**E and F**) Representative plot of granzyme B-expressing T cells at day 7 post expansion (**E**) and summary of T cells in granzyme B expression from data of two independent experiments (**F**). Error bars indicate mean ± SEM.

(**G**) Multifunctional cytokine expression of $CD3^+$ $CD8^+$ T or $CD3^+$ $CD4^+$ T cells at day 7 and day 11 post expansion.

(**H**) Resting $CD4^+$ T cells were sorted and spiked into CellTrace dye-labeled T cell products (day 13) at the indicated ratio and co-stimulated (cells to beads = 1 : 1) for 4 days. Duplicates for each group were performed. Cells were counted at day 4 before collection for anti-CD4-BV786 staining and analysis by flow cytometer. Cell counts were normalized to cell group without newly added $CD4^+$ T. Unpaired two-tailed *t*-test between two groups was performed. Error bars indicate mean ± SEM.

See also **Figure S7**.

DISCUSSION

TRuST provides a novel method that enables label-free reconstitution of lymphocyte subpopulations using the intrinsic side-scattering property of cells. We demonstrate that less-differentiated T cells are endowed with a lower SSC intensity, which, together with a high ratio of CD4/CD8 T cells, can be effectively enriched and used for optimum

T cell production (**Figures 2 and 4**). Furthermore, we address that both naïve T cells and a higher $CD4^+$ T to $CD8^+$ T proportion are critical for maximal $CD8^+$ T cells expansion and optimal $CD8^+$ T memory precursors maintenance (**Figures 5-7**).

Naïve T cells have discernable morphological profiles from memory/effector T cells under transmission electron microscope (Dimeloe et al., 2016). Our work demonstrates that this difference can be recaptured simply by using the side-scattering property, which would be more practically meaningful in a high-throughput and cost-effective manner. We showed that SSC is a robust biophysical attribute, the distribution pattern of which presents the intrinsic granularity difference of cellular context and is unaffected by either sample processing or voltage changes applied during data acquisition (**Figures S3A-S3D**). Thus, when applying the gate settings determined using pre-stained cell samples to the unstained cell samples, no gating normalization is required for T cell reconstitution by manual gate selection (**Figures 2 and 4)** and only slight gating correction is required for cell type purification by computational gate search (**Figure 3**). With a single sorting step based on the SSC intensity, lymphocyte populations with high $CD4^+$ T to $CD8^+$ T ratio are clustered together with younger T cells (e.g. T_N and early T_{CM}) among the cells of lower SSC. This strategy has been described to meet the demands of current T cell manufacturing procedures in both quantity and quality (**Figures 4, S4, and S5**). A significantly higher yield of T cell with more memory precursors can be achieved from the sorted SSC^{low} cell population. In addition, a comparable amount of T cells with stronger immediate effector function due

609 to the production of late-differentiated effector cells, can also be obtained from the
610 SSC^{high} cluster when compared to unfractionated total lymphocytes. On the other hand,
611 the majority of NK cells can be assigned to SSC^{high} population, which would be useful
612 if antibody-free methods are preferred for NK cells segregation (Hu et al., 2019).
613
614 Apheresis materials with high baseline T cell dysfunction (LAG-3^{+}/TNF-α^{low} $CD8^{+}$ T)
615 before cell manufacturing was reported to correlate with the non-responding rate of B-
616 CLL patients while a more memory-like functional profile predicts better response
617 (Finney et al., 2019). Similarly, sustained disease remission in B-cell acute
618 lymphoblastic leukemia (B-ALL) patients was associated with memory-like $CD27^{+}$
619 $CD45RO^{-}$ $CD8^{+}$ T cells before CAR T engineering (Fraietta et al., 2018). Interestingly,
620 we observed that T cell progenies derived from SSC^{low} group have significantly
621 accumulated $CD8^{+}$ $T_{CMRA\text{-}hi}$ subpopulation, which is endowed with naïve-like cytokine
622 expression profile (**Figures 4G-4I, S5C, and S5D**) and increased co-stimulatory
623 markers CD27/CD28 but reduced CD45RO/LAG-3 especially during the early
624 expansion phases (**Figures 4F and S5B**). This finding is of great interest for further
625 studies. In addition, tumor histology heterogeneity (e.g. tumor burden and anatomic
626 distribution) and T cell immunosuppression/persistency mechanisms play important
627 roles in cancer immunity and treatment (Majzner and Mackall, 2019). Here we
628 conceive a sequential infusion regimen, that combines highly potential effector cells
629 (SSC^{high}-derived) to immediately mitigate tumor load and followed by less-
630 differentiated cells (SSC^{low}-derived) to improve long-term tumor surveillance. However,

it remains to be validated whether such a treatment regimen would be more efficacious in refractory tumors aimed to maximally alleviate side effects (e.g. cytokine-releasing syndrome and neurotoxicity) while preventing huge tumor burden-caused T cell over-activation/exhaustion. The work has demonstrated its feasibility by producing adequate cell doses but with distinctive cellular quality from one packet of apheresis product.

Great efforts have been put into improving T cell manufacturing processes for better immunotherapy. For example, shortening the time frame of T cell expansion from around two weeks (Jacoby et al., 2019) to a few days (Ghassemi et al., 2018; Lu et al., 2016; Tu et al., 2019) or even without expansion in so called FasT CAR-T technology (Zhang et al., 2019). While more clinical data is required, both strategies have been proposed to maximally maintain the younger T cell subpopulations with enhanced engraftment and persistence. The use of homeostatic cytokine cocktails (e.g. IL-7/IL-15) (Surh and Sprent, 2008) or antigen-specific stimulation to maintain pools of less-differentiated T cells (e.g. T_{CM}/T_{SCM}) (Cieri et al., 2013; Xu et al., 2014) has also been described. Additionally, $CD4^+$ T or $CD8^+$ T cells or $CD8^+$ T_{CM} subset can be magnetically pre-enriched and expanded separately in the presence of optimal cytokine cocktails, and co-transfusion of $CD4^+$ T and $CD8^+$ T cell products has seen preliminary success in both manufacturing and therapeutic studies (Gardner et al., 2017; Shah et al., 2020; Sommermeyer et al., 2016; Turtle et al., 2016). $CD4^+$ T help is critical for optimal $CD8^+$ T expansion and early central memory pool maintenance in the absence of specific

653 cognate antigens (**Figures 6 and 7**). Hence, it will be of great interest to study how the
654 pre-reconstituted $CD4^+$ T/$CD8^+$ T cells before expansion may further improve
655 therapeutic efficacy when combined with the defined ratio of CD4/CD8 T cells for
656 infusion. This would be more practically meaningful considering that patients with some
657 tumors or chronic diseases tend to manifest a decreased ratio of CD4/CD8 T cells
658 (Patel et al., 2016; Sommermeyer et al., 2016; You et al., 2009). On the other hand,
659 rapid expansion method (REM), which requires large amount of non-dividing feeder
660 cells such as irradiated allogeneic PBMC or antigen-bearing lymphoblastoid cell line
661 (LCL), has been used to quickly obtain large numbers of therapeutic T cells (Jin et al.,
662 2018; Wang and Riviere, 2015). Our findings would provide an alternative approach to
663 achieve this without the use of additional feeder cells where only a proper ratio of $CD4^+$
664 T to $CD8^+$ T cells is adopted for co-expansion. Given these research progresses, our
665 method can be flexibly adapted into those manufacturing workflows.
666
667 There are two main advantages for the technical feasibility of TRuST for the
668 preparation of clinical grade T cell products. (1) The lack of expensive staining reagents
669 can significantly reduce cost. By using only one laser (e.g. Blue laser 488 nm) for
670 generating forward-scatter and side-scatter, data-processing burden during real-time
671 sorting can also be simplified. (2) The successful application of good manufacturing
672 practice (GMP)-compliant multiparameter flow cytometry systems in cell therapy
673 (**Table S1**) (Bluestone et al., 2015; Fritsche et al., 2020) and advances in microfluidic
674 systems enabling total lymphocytes enrichment immediately from whole blood in a

675 high-throughput approach by combining acoustic (Ding et al., 2013) and hydrodynamic
676 focusing (Lissandrello et al., 2018; Urbansky et al., 2017). Thus, we envisage the
677 versatility of side scatter-based lymphocytes analysis and reconstitution in these
678 platforms.
679
680 **Limitations**
681 Despite the simplicity and ingenuity associated with TRuST, a limitation of this strategy
682 is that it may not be feasible to discriminate differentiated lymphocyte subsets under
683 fast expansion due to confounding effects from enlarged cell size. A possible solution
684 could be the use of longer scattering wavelengths. Also, studies are required in future
685 to test how efficient the SSC-based lymphocyte segregation is when using patient
686 samples which usually manifest abnormal lymphocytes composition and activation
687 statuses. We have demonstrated that it is of adequate sensitivity and pronounced
688 usefulness to segregate the majority of naïve T cells from more-differentiated T cell
689 subsets with controllable CD4/CD8 T cells ratio. We have also showed that, it is
690 feasible to enhance the purification of specific lymphocyte subsets via computational
691 gate design. Nevertheless, it would be more powerful for other applications such as
692 label-free disease diagnosis and highly purified cell selection if the scattering resolution
693 was further improved with interdisciplinary efforts. For example, use of microchannel-
694 based fluidic systems and adoption of adjustable scattering angles (Rossi et al., 2019),
695 inclusion of generic dyes (e.g. MitoTracker) measuring mitochondrial
696 abundance/activity (Baron et al., 2019), or biomarkers possibly surrogating biophysical

properties (Tsai et al., 2020; Walsh et al., 2019) to improve lymphocyte subsets identification.

Overall, TRuST is a reliable and effective approach for optimum T cell reconstitution, that will be a significant improvement for current cell manufacturing methods. TRuST is also feasible for the selection of specific lymphocyte subsets for lymphocyte biology studies. This work has provided new insights into the intrinsic light-scattering attributes of different lymphocytes and will pave the way for the improvement and broad application of light property-relied cell identification and separation with interdisciplinary efforts.

SUPPLEMENTARY INFORMATION

Supplementary information is available for this manuscript.

ACKNOWLEDGEMENTS

This work was supported by funding from NUS Research Scholarship and Institute for Health Innovation and Technology (iHealthtech), NUS. The authors acknowledge technical support from the Flow Cytometry Laboratory (NUS Medical Sciences Cluster) for cell sorting.

AUTHOR CONTRIBUTIONS

T.W and L.F.C conceived and designed the study. T.W performed the experiments and

data analysis with all other authors' assistance. T.W and L.F.C wrote the manuscript. Y.H.L, Y.L, and H.J.W reviewed the manuscript and provided feedback. All authors commented on the manuscript and approved the submission.

DECLARATION OF INTERESTS

The authors declare no competing interests.

REFERENCES

Alspach, E., Lussier, D.M., Miceli, A.P., Kizhvatov, I., DuPage, M., Luoma, A.M., Meng, W., Lichti, C.F., Esaulova, E., Vomund, A.N., *et al.* (2019). MHC-II neoantigens shape tumour immunity and response to immunotherapy. Nature *574*, 696-701.

Arina, A., Karrison, T., Galka, E., Schreiber, K., Weichselbaum, R.R., and Schreiber, H. (2017). Transfer of Allogeneic CD4+ T Cells Rescues CD8+ T Cells in Anti-PD-L1-Resistant Tumors Leading to Tumor Eradication. Cancer Immunol Res *5*, 127-136.

Attanasio, J., and Wherry, E.J. (2016). Costimulatory and Coinhibitory Receptor Pathways in Infectious Disease. Immunity *44*, 1052-1068.

Baron, C.S., Barve, A., Muraro, M.J., van der Linden, R., Dharmadhikari, G., Lyubimova, A., de Koning, E.J.P., and van Oudenaarden, A. (2019). Cell Type Purification by Single-Cell Transcriptome-Trained Sorting. Cell *179*, 527-542 e519.

Berger, C., Jensen, M.C., Lansdorp, P.M., Gough, M., Elliott, C., and Riddell, S.R. (2008). Adoptive transfer of effector CD8+ T cells derived from central memory cells establishes persistent T cell memory in primates. J Clin Invest *118*, 294-305.

Bluestone, J.A., Buckner, J.H., Fitch, M., Gitelman, S.E., Gupta, S., Hellerstein, M.K., Herold, K.C., Lares, A., Lee, M.R., Li, K., *et al.* (2015). Type 1 diabetes immunotherapy using polyclonal regulatory T cells. Science translational medicine *7*, 315ra189-315ra189.

Bohler, T., von Au, M., Klose, N., Muller, K., Coulibaly, B., Nauwelaers, F., Spengler, H.P., Kynast-Wolf, G., and Krausslich, H.G. (2007). Evaluation of a simplified dual-platform flow cytometric method for measurement of lymphocyte subsets and T-cell maturation phenotypes in the population of Nouna, Burkina Faso. Clinical and vaccine immunology : CVI *14*, 775-781.

Chen, L., and Flies, D.B. (2013). Molecular mechanisms of T cell co-stimulation and co-inhibition. Nat Rev Immunol *13*, 227-242.

Cieri, N., Camisa, B., Cocchiarella, F., Forcato, M., Oliveira, G., Provasi, E., Bondanza, A., Bordignon, C., Peccatori, J., Ciceri, F., *et al.* (2013). IL-7 and IL-15 instruct the generation of human memory stem T cells from naive precursors. Blood *121*, 573-584.

Clark, R.A., Shackelton, J.B., Watanabe, R., Calarese, A., Yamanaka, K., Campbell, J.J., Teague, J.E., Kuo, H.P., Hijnen, D., and Kupper, T.S. (2011). High-scatter T cells: a reliable biomarker for malignant

T cells in cutaneous T-cell lymphoma. Blood *117*, 1966-1976.

Cook, K.D., and Whitmire, J.K. (2013). The depletion of NK cells prevents T cell exhaustion to efficiently control disseminating virus infection. Journal of immunology *190*, 641-649.

Cossarizza, A., Chang, H.-D., Radbruch, A., Acs, A., Adam, D., Adam-Klages, S., Agace, W.W., Aghaeepour, N., Akdis, M., Allez, M., *et al.* (2019). Guidelines for the use of flow cytometry and cell sorting in immunological studies (second edition). European journal of immunology *49*, 1457-1973.

Deng, Q., Han, G., Puebla-Osorio, N., Ma, M.C.J., Strati, P., Chasen, B., Dai, E., Dang, M., Jain, N., Yang, H., *et al.* (2020). Characteristics of anti-CD19 CAR T cell infusion products associated with efficacy and toxicity in patients with large B cell lymphomas. Nature medicine.

Denton, A.E., Russ, B.E., Doherty, P.C., Rao, S., and Turner, S.J. (2011). Differentiation-dependent functional and epigenetic landscapes for cytokine genes in virus-specific CD8+ T cells. Proceedings of the National Academy of Sciences of the United States of America *108*, 15306-15311.

Dimeloe, S., Mehling, M., Frick, C., Loeliger, J., Bantug, G.R., Sauder, U., Fischer, M., Belle, R., Develioglu, L., Tay, S., *et al.* (2016). The Immune-Metabolic Basis of Effector Memory CD4+ T Cell Function under Hypoxic Conditions. J Immunol *196*, 106-114.

Ding, X., Li, P., Lin, S.C., Stratton, Z.S., Nama, N., Guo, F., Slotcavage, D., Mao, X., Shi, J., Costanzo, F., *et al.* (2013). Surface acoustic wave microfluidics. Lab on a chip *13*, 3626-3649.

Finney, O.C., Brakke, H.M., Rawlings-Rhea, S., Hicks, R., Doolittle, D., Lopez, M., Futrell, R.B., Orentas, R.J., Li, D., Gardner, R.A., *et al.* (2019). CD19 CAR T cell product and disease attributes predict leukemia remission durability. J Clin Invest *129*, 2123-2132.

Fraietta, J.A., Lacey, S.F., Orlando, E.J., Pruteanu-Malinici, I., Gohil, M., Lundh, S., Boesteanu, A.C., Wang, Y., O'Connor, R.S., Hwang, W.T., *et al.* (2018). Determinants of response and resistance to CD19 chimeric antigen receptor (CAR) T cell therapy of chronic lymphocytic leukemia. Nature medicine *24*, 563-571.

Fritsche, E., Volk, H.D., Reinke, P., and Abou-El-Enein, M. (2020). Toward an Optimized Process for Clinical Manufacturing of CAR-Treg Cell Therapy. Trends Biotechnol *38*, 1099-1112.

Fuertes Marraco, S.A., Soneson, C., Cagnon, L., Gannon, P.O., Allard, M., Abed Maillard, S., Montandon, N., Rufer, N., Waldvogel, S., Delorenzi, M., *et al.* (2015). Long-lasting stem cell-like memory CD8+ T cells with a naive-like profile upon yellow fever vaccination. Science translational medicine *7*, 282ra248.

Gardner, R.A., Finney, O., Annesley, C., Brakke, H., Summers, C., Leger, K., Bleakley, M., Brown, C., Mgebroff, S., Kelly-Spratt, K.S., *et al.* (2017). Intent-to-treat leukemia remission by CD19 CAR T cells of defined formulation and dose in children and young adults. Blood *129*, 3322-3331.

Gattinoni, L., Klebanoff, C.A., Palmer, D.C., Wrzesinski, C., Kerstann, K., Yu, Z., Finkelstein, S.E., Theoret, M.R., Rosenberg, S.A., and Restifo, N.P. (2005). Acquisition of full effector function in vitro paradoxically impairs the in vivo antitumor efficacy of adoptively transferred CD8+ T cells. J Clin Invest *115*, 1616-1626.

Gattinoni, L., Lugli, E., Ji, Y., Pos, Z., Paulos, C.M., Quigley, M.F., Almeida, J.R., Gostick, E., Yu, Z., Carpenito, C., *et al.* (2011). A human memory T cell subset with stem cell-like properties. Nature medicine *17*, 1290-1297.

Ghassemi, S., Nunez-Cruz, S., O'Connor, R.S., Fraietta, J.A., Patel, P.R., Scholler, J., Barrett, D.M., Lundh, S.M., Davis, M.M., Bedoya, F., *et al.* (2018). Reducing Ex Vivo Culture Improves the Antileukemic Activity of Chimeric Antigen Receptor (CAR) T Cells. Cancer Immunol Res *6*, 1100-1109.

Grutzkau, A., and Radbruch, A. (2010). Small but mighty: how the MACS-technology based on nanosized superparamagnetic particles has helped to analyze the immune system within the last 20 years.

Cytometry A *77*, 643-647.

Hinrichs, C.S., Borman, Z.A., Cassard, L., Gattinoni, L., Spolski, R., Yu, Z., Sanchez-Perez, L., Muranski, P., Kern, S.J., Logun, C., *et al.* (2009). Adoptively transferred effector cells derived from naive rather than central memory CD8+ T cells mediate superior antitumor immunity. Proceedings of the National Academy of Sciences of the United States of America *106*, 17469-17474.

Hinrichs, C.S., Borman, Z.A., Gattinoni, L., Yu, Z., Burns, W.R., Huang, J., Klebanoff, C.A., Johnson, L.A., Kerkar, S.P., Yang, S., *et al.* (2011). Human effector CD8+ T cells derived from naive rather than memory subsets possess superior traits for adoptive immunotherapy. Blood *117*, 808-814.

Hu, W., Wang, G., Huang, D., Sui, M., and Xu, Y. (2019). Cancer Immunotherapy Based on Natural Killer Cells: Current Progress and New Opportunities. Frontiers in immunology *10*, 1205.

Jacoby, E., Shahani, S.A., and Shah, N.N. (2019). Updates on CAR T-cell therapy in B-cell malignancies. Immunol Rev *290*, 39-59.

Jin, J., Gkitsas, N., Fellowes, V.S., Ren, J., Feldman, S.A., Hinrichs, C.S., Stroncek, D.F., and Highfill, S.L. (2018). Enhanced clinical-scale manufacturing of TCR transduced T-cells using closed culture system modules. Journal of translational medicine *16*, 13.

Klebanoff, C.A., Scott, C.D., Leonardi, A.J., Yamamoto, T.N., Cruz, A.C., Ouyang, C., Ramaswamy, M., Roychoudhuri, R., Ji, Y., Eil, R.L., *et al.* (2016). Memory T cell-driven differentiation of naive cells impairs adoptive immunotherapy. J Clin Invest *126*, 318-334.

Laghmouchi, A., Hoogstraten, C., Falkenburg, J.H.F., and Jedema, I. (2020). Long-term in vitro persistence of magnetic properties after magnetic bead-based cell separation of T cells. Scand J Immunol *92*, e12924.

Lissandrello, C., Dubay, R., Kotz, K.T., and Fiering, J. (2018). Purification of Lymphocytes by Acoustic Separation in Plastic Microchannels. SLAS Technol *23*, 352-363.

Loudon, W.G., Abraham, S.R., Owen-Schaub, L.B., Hemingway, L.L., Hemstreet, G.P., and DeBault, L.E. (1988). Identification and selection of human lymphokine activated killer cell effectors and novel recycling intermediates by unique light-scattering properties. Cancer Res *48*, 2184-2192.

Lu, T.L., Pugach, O., Somerville, R., Rosenberg, S.A., Kochenderfer, J.N., Better, M., and Feldman, S.A. (2016). A Rapid Cell Expansion Process for Production of Engineered Autologous CAR-T Cell Therapies. Human gene therapy methods *27*, 209-218.

Majzner, R.G., and Mackall, C.L. (2019). Clinical lessons learned from the first leg of the CAR T cell journey. Nature medicine *25*, 1341-1355.

Nakanishi, Y., Lu, B., Gerard, C., and Iwasaki, A. (2009). CD8(+) T lymphocyte mobilization to virus-infected tissue requires CD4(+) T-cell help. Nature *462*, 510-513.

Ojaghi, A., Carrazana, G., Caruso, C., Abbas, A., Myers, D.R., Lam, W.A., and Robles, F.E. (2020). Label-free hematology analysis using deep-ultraviolet microscopy. Proceedings of the National Academy of Sciences of the United States of America *117*, 14779-14789.

Patel, S., Jones, R.B., Nixon, D.F., and Bollard, C.M. (2016). T-cell therapies for HIV: Preclinical successes and current clinical strategies. Cytotherapy *18*, 931-942.

Plouffe, B.D., Murthy, S.K., and Lewis, L.H. (2015). Fundamentals and application of magnetic particles in cell isolation and enrichment: a review. Rep Prog Phys *78*, 016601.

Radtke, S., Pande, D., Cui, M., Perez, A.M., Chan, Y.-Y., Enstrom, M., Schmuck, S., Berger, A., Eunson, T., Adair, J.E., *et al.* (2019). Sort-purification of human CD34+ CD90+ cells reduces target cell population and improves lentiviral transduction. bioRxiv, 850479.

Rafiq, S., Hackett, C.S., and Brentjens, R.J. (2020). Engineering strategies to overcome the current

roadblocks in CAR T cell therapy. Nature reviews Clinical oncology *17*, 147-167.

Roddie, C., O'Reilly, M., Dias Alves Pinto, J., Vispute, K., and Lowdell, M. (2019). Manufacturing chimeric antigen receptor T cells: issues and challenges. Cytotherapy *21*, 327-340.

Rossi, D., Dannhauser, D., Telesco, M., Netti, P.A., and Causa, F. (2019). CD4+ versus CD8+ T-lymphocyte identification in an integrated microfluidic chip using light scattering and machine learning. Lab on a chip *19*, 3888-3898.

Ruban, G.I., Berdnik, V.V., Marinitch, D.V., Goncharova, N.V., and Loiko, V.A. (2010). Light scattering and morphology of the lymphocyte as applied to flow cytometry for distinguishing healthy and infected individuals. J Biomed Opt *15*, 057008.

Schietinger, A., Philip, M., Liu, R.B., Schreiber, K., and Schreiber, H. (2010). Bystander killing of cancer requires the cooperation of CD4(+) and CD8(+) T cells during the effector phase. The Journal of experimental medicine *207*, 2469-2477.

Seder, R.A., and Ahmed, R. (2003). Similarities and differences in CD4+ and CD8+ effector and memory T cell generation. Nature immunology *4*, 835-842.

Shah, N.N., Highfill, S.L., Shalabi, H., Yates, B., Jin, J., Wolters, P.L., Ombrello, A., Steinberg, S.M., Martin, S., Delbrook, C.*, et al.* (2020). CD4/CD8 T-Cell Selection Affects Chimeric Antigen Receptor (CAR) T-Cell Potency and Toxicity: Updated Results From a Phase I Anti-CD22 CAR T-Cell Trial. J Clin Oncol *38*, 1938-1950.

Sommermeyer, D., Hudecek, M., Kosasih, P.L., Gogishvili, T., Maloney, D.G., Turtle, C.J., and Riddell, S.R. (2016). Chimeric antigen receptor-modified T cells derived from defined CD8+ and CD4+ subsets confer superior antitumor reactivity in vivo. Leukemia *30*, 492-500.

Stuart, T., Butler, A., Hoffman, P., Hafemeister, C., Papalexi, E., Mauck, W.M., 3rd, Hao, Y., Stoeckius, M., Smibert, P., and Satija, R. (2019). Comprehensive Integration of Single-Cell Data. Cell *177*, 1888-1902 e1821.

Sun, J.C., Williams, M.A., and Bevan, M.J. (2004). CD4+ T cells are required for the maintenance, not programming, of memory CD8+ T cells after acute infection. Nature immunology *5*, 927-933.

Surh, C.D., and Sprent, J. (2008). Homeostasis of naive and memory T cells. Immunity *29*, 848-862.

Teeman, E., Shasha, C., Evans, J.E., and Krishnan, K.M. (2019). Intracellular dynamics of superparamagnetic iron oxide nanoparticles for magnetic particle imaging. Nanoscale *11*, 7771-7780.

Terstappen, L.W., de Grooth, B.G., Nolten, G.M., ten Napel, C.H., van Berkel, W., and Greve, J. (1986a). Physical discrimination between human T-lymphocyte subpopulations by means of light scattering, revealing two populations of T8-positive cells. Cytometry *7*, 178-183.

Terstappen, L.W., De Grooth, B.G., Ten Napel, C.H., Van Berkel, W., and Greve, J. (1986b). Discrimination of human cytotoxic lymphocytes from regulatory and B-lymphocytes by orthogonal light scattering. J Immunol Methods *95*, 211-216.

Terstappen, L.W., de Grooth, B.G., van Berkel, W., ten Napel, C.H., and Greve, J. (1988). Application of orthogonal light scattering for routine screening of lymphocyte samples. Cytometry *9*, 220-225.

Tsai, A.G., Glass, D.R., Juntilla, M., Hartmann, F.J., Oak, J.S., Fernandez-Pol, S., Ohgami, R.S., and Bendall, S.C. (2020). Multiplexed single-cell morphometry for hematopathology diagnostics. Nat Med *26*, 408-417.

Tu, S., Huang, R., Guo, Z., Deng, L., Song, C., Zhou, X., Yue, C., Zhang, L., He, Y., Yang, J.*, et al.* (2019). Shortening the ex vivo culture of CD19-specific CAR T-cells retains potent efficacy against acute lymphoblastic leukemia without CAR T-cell-related encephalopathy syndrome or severe cytokine release syndrome. American journal of hematology *94*, E322-E325.

Turtle, C.J., Hanafi, L.A., Berger, C., Gooley, T.A., Cherian, S., Hudecek, M., Sommermeyer, D., Melville, K., Pender, B., Budiarto, T.M., *et al.* (2016). CD19 CAR-T cells of defined CD4+:CD8+ composition in adult B cell ALL patients. J Clin Invest *126*, 2123-2138.

Urbansky, A., Ohlsson, P., Lenshof, A., Garofalo, F., Scheding, S., and Laurell, T. (2017). Rapid and effective enrichment of mononuclear cells from blood using acoustophoresis. Sci Rep *7*, 17161.

van Leeuwen, E.M., Gamadia, L.E., Baars, P.A., Remmerswaal, E.B., ten Berge, I.J., and van Lier, R.A. (2002). Proliferation requirements of cytomegalovirus-specific, effector-type human CD8+ T cells. Journal of immunology *169*, 5838-5843.

Waller, E.C., McKinney, N., Hicks, R., Carmichael, A.J., Sissons, J.G., and Wills, M.R. (2007). Differential costimulation through CD137 (4-1BB) restores proliferation of human virus-specific "effector memory" (CD28(-) CD45RA(HI)) CD8(+) T cells. Blood *110*, 4360-4366.

Walsh, A., Mueller, K., Jones, I., Walsh, C.M., Piscopo, N., Niemi, N.N., Pagliarini, D.J., Saha, K., and Skala, M.C. (2019). Label-free Method for Classification of T cell Activation. bioRxiv, 536813.

Wang, X., Berger, C., Wong, C.W., Forman, S.J., Riddell, S.R., and Jensen, M.C. (2011). Engraftment of human central memory-derived effector CD8+ T cells in immunodeficient mice. Blood *117*, 1888-1898.

Wang, X., and Riviere, I. (2015). Manufacture of tumor- and virus-specific T lymphocytes for adoptive cell therapies. Cancer Gene Ther *22*, 85-94.

Xu, Y., Zhang, M., Ramos, C.A., Durett, A., Liu, E., Dakhova, O., Liu, H., Creighton, C.J., Gee, A.P., Heslop, H.E., *et al.* (2014). Closely related T-memory stem cells correlate with in vivo expansion of CAR.CD19-T cells and are preserved by IL-7 and IL-15. Blood *123*, 3750-3759.

You, J., Zhuang, L., Zhang, Y.F., Chen, H.Y., Sriplung, H., Geater, A., Chongsuvivatwong, V., Piratvisuth, T., McNeil, E., Yu, L., *et al.* (2009). Peripheral T-lymphocyte subpopulations in different clinical stages of chronic HBV infection correlate with HBV load. World J Gastroenterol *15*, 3382-3393.

Zeskind, B.J., Jordan, C.D., Timp, W., Trapani, L., Waller, G., Horodincu, V., Ehrlich, D.J., and Matsudaira, P. (2007). Nucleic acid and protein mass mapping by live-cell deep-ultraviolet microscopy. Nat Methods *4*, 567-569.

Zhang, C., He, J., Liu, L., Wang, J., Wang, S., Liu, L., Gao, L., Gao, L., Liu, Y., Kong, P., *et al.* (2019). CD19-Directed Fast CART Therapy for Relapsed/Refractory Acute Lymphoblastic Leukemia: From Bench to Bedside. Blood *134*, 1340-1340.

Zhang, C., Wang, Z., Yang, Z., Wang, M., Li, S., Li, Y., Zhang, R., Xiong, Z., Wei, Z., Shen, J., *et al.* (2017). Phase I Escalating-Dose Trial of CAR-T Therapy Targeting CEA(+) Metastatic Colorectal Cancers. Mol Ther *25*, 1248-1258.

METHODS

Reagents

Apheresis residual blood cones were collected from healthy adult donors from the Health Sciences Authority (HSA), Singapore, with approval from Institutional Review Board and informed consent from donors (NUS-IRB no. H-18-038E). Ficoll® Paque

Plus (GE Healthcare, 17-1440-02) was used for peripheral blood mononuclear cells (PBMC) enrichment. Cell culture medium RPMI1640 (Gibco, A1049101) supplemented with heat-inactivated fetal bovine serum (FBS) (Gibco, 10270106) was used for primary cell culture. In some experiments, anti-CD3/CD28 Dynabeads™ (Gibco, 11161D) were used for T cell activation and expansion in the condition of human recombinant IL-2 (Gibco, PHC0021) or where indicated, human recombinant IL-7 plus IL-15. Phorbol ester (PMA) (Sigma-Aldrich, P8139) and ionomycin (Sigma-Aldrich, I9657) were used for cell stimulation to produce cytokines. Cytofix/Cytoperm™ reagent kit (BD Biosciences, 554714) was used for cell fixation and permeabilization before intracellular staining. Flow cytometry antibodies used in this study are listed as follows. Antibodies from BD Biosciences include: CD3-BUV395 (Clone UCHT1; cat #563546), CD4-BV786 (Clone SK3; cat #563877) and CD8-PE-Cy7 (Clone SK1; cat #335787). Antibodies from Biolegend include: CD3-FITC (Clone UCHT1; cat #300406), CCR7-PE (Clone G043H7; cat #353204), CD45RA-APC (Clone HI100; cat #304112), CD45RO-Pacific Blue (Clone UCHL1; cat #304215),CD27-Pacific Blue (Clone M-T271; cat #356413), CD28-FITC (Clone CD28.2; cat #302906), CD95-FITC (Clone DX2; cat #305605), CD127-Brilliant Violet 785 (Clone A019D5; cat #351329), TIM-3-Pacific Blue (Clone F38-2E2; cat #345041), CD57-FITC (Clone HNK-1; cat #359603), LAG-3-Brilliant Violet 785 (Clone 11C3C65; cat #369321) and human TruStain FcX reagent (Cat #422302). Antibodies for intracellular staining include granzyme B-PE (BD Biosciences, GB11; cat #561142), IFN-γ-FITC (Miltenyi Biotec, cat #130-090-433), IL-2-PE (Miltenyi Biotec, cat #130-090-487) and TNF-α-APC (Miltenyi Biotec, cat #130-

091-267).

PBMC isolation and usage

PBMC were isolated from apheresis blood of healthy donors by density gradient centrifugation. To ensure batch-to-batch consistency, the enriched PBMC were counted and cryopreserved at 10 million cells/vial using liquid nitrogen and medium containing 90% FBS and 10% DMSO. For each experiment, the cells were recovered overnight in RPMI1640 supplemented with 10% FBS before downstream experiments.

T cell differentiation lineages and phenotypes characterization

In this study, two gating methods were used to identify T cell differentiation lineages. For resting T cells, based on the expression level of canonical markers CCR7/CD45RA/CD45RO, they can be broadly classified as naïve (T_N, $CD45RA^{high}$ $CCR7^{high}$ $CD45RO^{-}$), central memory (T_{CM}, $CD45RA^{dim/-}$ $CCR7^{low}$), effector memory (T_{EM}, $CD45RA^{dim/-}$ $CCR7^{-}$) and terminally differentiated effector (T_{EMRA}, $CD45RA^{high}$ $CCR7^{-}$) (Bohler et al., 2007; Seder and Ahmed, 2003). For T cells undergoing activation and proliferation, an in-depth gating strategy was adapted where the T_{CM} is further dissected into naïve phenotype-closest $CD45RA^{high}$ T_{CM} ($T_{CMRA\text{-}hi}$), memory phenotype-closest $CD45RA^{low}$ T_{CM} ($T_{CMRA\text{-}low}$) and $CD45RA^{-}$ T_{CM} (T_{CMO}), while T_{EM} with CD45RA expression is classified into $CD45RA^{low}$ T_{EM} ($T_{EMRA\text{-}low}$) and $CD45RA^{high}$ T_{EM} ($T_{EMRA\text{-}hi}$).

To better understand the T cell dynamic changes in their activation/senescent statuses

either before or during expansion, the expression profile of a panel of selected cell surface markers was longitudinally assessed, and it includes classical naïve/memory markers CCR7/CD45RA/CD45RO, proliferation and survival-enhancing costimulatory receptors CD27/CD28, and immune activation/inhibition markers CD127/CD95/CD57/LAG-3/TIM-3. To mitigate compensation-induced mutual signaling interferences in multiparameter flow cytometry, the staining panels were designed as follows: panel for dynamic change of naïve/memory composition (CD3-FITC/CD4-BV786/CD8-PE-Cy7/CCR7-PE/CD45RA-APC/CD45RO-V450), panel for co-expression of co-stimulatory markers in naïve/memory subsets (CD3-BUV395/CD8-PE.Cy7/CCR7-PE/CD45RA-APC/CD27-Pacific Blue/CD28-FITC), two panels were designed for immune activation/inhibition markers profiling in naïve/memory T cell subsets (CD3-BUV395/CD8-PE-Cy7/CCR7-PE/CD45RA-APC/CD45RO-Pacific Blue /CD95-FITC/CD127-BV785, or CD3-BUV395/CD8-PE-Cy7/CCR7-PE/CD45RA-APC /TIM-3-Pacific Blue/CD57-FITC/LAG-3-BV785). Pre-blocking step with TruStain FcX (BioLegend) was included for all staining. For some experiments where significant dead cells may be generated such as the first 2-3 days post T cell activation and PMA-based stimulation, LIVE/DEAD viability dye (Invitrogen, L34963) was used to exclude dead cells. CD3-FITC, CD4-BV786, and CD8-PE-Cy7 were from BD Biosciences. All other antibodies used were purchased from BioLegend . Flow cytometry compensation matrices and sample data acquisition were completed in CytoFLEX analyzer (Beckman Coulter) and analyzed by FlowJo software version 10.

Light-scattering distribution of lymphocytes

To obtain the light-scattering profile of main lymphocyte populations and subpopulations, PBMC were rested overnight, and stained with CD3-BUV395/CD4-BV786/CD8-PE-Cy7 for T cell population identification, or CD3-BUV395/CD56-BV786/CD19-FITC for NK and B cell identification, or CD3-BUV395/CD4-BV786/CD8-PE-Cy7/CCR7-PE/CD45RA-APC for naïve/memory T cells characterization. After washing, the cells were re-suspended in cold PBS before flow cytometry data acquisition. For a label-free approach, the cells were washed twice in cold phosphate buffer (PBS) before suspended in cold PBS and sorted on Moflo Astrios (Beckman Coulter). Sorted cells with different scattering intensity were stained to identify the percentages of $CD3^+$ $CD4^+$ T/$CD3^+$ $CD8^+$ T, NK/B cell, or T_N/T_{CM}/T_{EM}/T_{EMRA}. Where indicated, a panel of selected surface markers was included to probe the detailed activation/senescent phenotypes of sorted cell populations, including CD45RO, CD27, CD28, CD127, CD95, CD57, LAG-3 and TIM-3. The scattering plots were generated by FlowJo software.

Lymphocytes enrichment by automatic gating search

Computational gating search (GateID) (Baron et al., 2019) was used to find the gate for optional cell type enrichment from a mixed cell population. Briefly, PBMC were recovered overnight and stained with different antibody panels for T cell identification (CD3-BUV395/CD4-BV786/CD8-PE-Cy7), NK/B cells identification (CD3-BUV395/CD56-BV786/CD19-FITC), or naïve/memory T cells characterization (CD3-

BUV395/CD4-BV786/CD8-PE-Cy7/CCR7-PE/CD45RA-APC). After washing, flow cytometry data was acquired in CytoFLEX analyzer (Beckman Coulter). The raw readouts corresponding to FSC and SSC parameters for each cell type were exported and input into the GateID package. The yield for each desired cell type (e.g. $CD4^+$ T/$CD8^+$ T/NK/B/T_N/T_{CM}/T_{EM}/T_{EMRA}) was set to 5% - 100 % and gating vertices were constantly set to 4. The yield is the count percentage of target cell type within the gating to that of the whole cell population, while the purity indicates the proportion of target cell type to total cell numbers within each gate corresponding to desired yield.

Cell sorting

For light-scatter based label-free cell sorting from resting PBMC, cryopreserved PBMC were recovered overnight in RPMI1640 supplemented with 10% FBS and washed in cold phosphate buffer (PBS) before suspended in cold PBS and sorted on Moflo Astrios (Beckman Coulter). The excitation wavelength for the generation of side-scatter (488/6-nm filter) and forward-scatter (488/6-nm filter) was 488 nm. Where indicated, a combined excitation by 488 nm and 405 nm was adopted to sort lymphocytes of different side-scatter (488/6-nm and 405/10-nm filter). Side-scatter was measured at an orthogonal angle from the light beam propagation axis while forward-scatter was measured anti-parallel to the incident beam. To make batch-to-batch experiments comparable, the sorting gate was set to equally sort cell populations of different light intensity (SSC^{high}/SSC^{low} or FSC^{high}/FSC^{low}). For antibody staining-based cell sorting, PBMC were pre-blocked with TruStain FcX and stained with CD4-BV786

(BD Biosciences) and CD8-PE-Cy7 (BD Biosciences) for sequential sorting of $CD4^+$ cells and $CD8^+$ cells on Moflo Astrios. It is important to note that only the cells with the high expression of CD8 were sorted as $CD8^+$ T cells because there were some NK cells that also expressed diminished CD8. Also, anti-CD3 was not used for cell sorting experiments where the sorted cells would be subjected to CD3/CD28-engaged stimulation. The sorted cells were validated to achieve enough purity of $CD3^+$ $CD4^+$ T or $CD3^+$ $CD8^+$ T cells (> 97%) before reconstituted for co-culture assay.

Cell stimulation and expansion in vitro

Sorted SSC^{low} and SSC^{high} cells were either expanded alone or reconstituted at a ratio of 1:1 (equal to total lymphocytes within initial cell sample) for co-expansion. The starting cell numbers for each condition were 0.08 million/well in 96-well plate. After 1-hour incubation at 37°C, all cell groups were activated by CD3/CD28 engagement at anti-CD3/CD28 microbeads to cells ratio 3:1 and 5 ng/ml IL-2. Similarly, the sorted $CD4^+$ T cells and $CD8^+$ T cells were reconstituted at indicated ratios to achieve 0.06 million/well. The ratio of anti-CD3/CD28 microbeads to cells was 3:1 and 5 ng/ml of IL-2 was supplemented. Half of the culture medium was replaced with fresh medium containing 5 ng/ml IL-2 every two days during initial activation/expansion stages (day 3 to day 7) and daily during late expansion phases (day 7 to day 11). During the expansion course, the cell numbers in each group were counted by trypan blue exclusion and aliquoted into approximately 0.1 million/well for all groups to mitigate high cell concentration. Data collection included manual counting of total nucleated

cells (TNC), flow cytometry detection of CD4/CD8 T cells, effector/memory composition, and effectors expression (e.g. cytokines and granzyme B) at indicated time points post activation.

Around 5 million expanded T cells at day 11 for each condition were cryopreserved for future usage. In some experiments where cell responsiveness to second stimulation was tested by CD3/CD28 engagement, the pre-expanded T cells at day 11 derived from different SSC groups were thawed and incubated at 37°C overnight. 0.06 million cells were seeded into each well of a 96-well plate and re-stimulated by anti-CD3/CD28 microbeads at beads to cell ratio of 1:1 under 5 ng/ml IL-2 or 5 ng/ml IL-7 and 5 ng/ml IL-15. Total cell numbers were recorded by manual counting and split into approximately 0.1 million/well to minimize high cell concentration. To assess the ability of $CD4^+$ T cells to rescue the proliferation capability of extensively pre-expanded $CD8^+$ T cells, cell materials derived from SSC^{high} group (day 13) which was enriched in large numbers of terminally differentiated $CD8^+$ T cells were labelled with CellTrace Far Red (Invitrogen, C34564) following the manufacturer protocol. The labelled T cells and sorted resting $CD4^+$ T cells of the same donor were reconstituted at indicated ratios and activated by anti-CD3/CD28 microbeads supplemented with 5 ng/ml IL-2. After 4 days, total cell numbers were counted and stained with CD4-BV786 before analysis on flow cytometer to determine $CD8^+$ T cells proliferation.

Functionality in effecting factors expression

To determine the immune response of T cells in cytokine and granzyme B expression, residual anti-CD3/CD28 microbeads were removed from expanded T cells at day 7 or day 11 before being re-stimulated in the presence or absence of 50 ng/ml PMA and 1 μg/ml ionomycin for an additional 2.5 hours. Cells were collected and labelled with LIVE/DEAD viability dye before further blocking with TruStain FcX. Surface markers CD3-BUV395 and CD8-PE-Cy7 were used to characterize T cell populations. After fixation/permeabilization treatment, each sample was divided into two tubes for either cytokine detection with IFN-γ-FITC (Miltenyi Biotec), IL-2-PE (Miltenyi Biotec) and TNF-α-APC (Miltenyi Biotec) or granzyme B measurement with granzyme B-PE (BD Biosciences) where isotype control antibodies were properly included. Flow cytometry data were acquired in CytoFLEX analyzer (Beckman Coulter) and analyzed by FlowJo software. Notably, the CD4 marker has a substantial downregulation post PMA stimulation, thus the $CD3^+$ $CD8^-$ T cells were gated as $CD3^+CD4^+$ T cells instead for data presentation.

Migration assay

In vitro chemotactic migration was used to evaluate the cells lymphnode-homing capacity. Briefly, CCL19 (300 ng/ml) and CCL21 (300 ng/ml) (PeproTech) in 100 μl culture medium were added to the lower chamber of 96-well transwell plate (5 μm porosity) (Corning, CLS3388). For control group, only culture medium without chemokines was added. 0.1 million expanded T cells (day 11) derived from SSC^{high}, SSC^{low} and reconstituted $SSC^{high+low}$ groups, or from experiments using $CD4^+$ T-$CD8^+$

T co-culture were seeded into the upper chamber in 80 µl culture medium. Each condition was conducted in duplicates. After five hours, the numbers of cells migrating to the lower chamber were counted by trypan blue exclusion. For migration capacity, the counts subtracted from the migrated cell numbers in control group were presented, correspondingly.

Principal component analysis

For each cell sample derived from sorted SSC^{high}, SSC^{low} or reconstituted $SSC^{high+low}$ population, the cell composition (T_N, $T_{CMRA\text{-}hi}$, $T_{CMRA\text{-}low}$, $T_{CMRA\text{-}low}$, T_{CMO}, T_{EM}, $T_{EMRA\text{-}hi}$, and $T_{EMRA\text{-}low}$) and multifunctional cytokine expression profile (IFN-γ^+ only, IL-2^+ only, TNF-α^+ only, IFN-γ^+ IL-2^+, IFN-γ^+ TNF-α^+, IL-2^+ TNF- α^+, and IFN-γ^+ IL-2^+ TNF-α^+) were integrated together for PCA calculation using the program embedded in Seurat package (Stuart et al., 2019). For PCA plotting, the same cell subsets from all groups with percentage less than 4% were omitted. The data for day 7 and day 11 were calculated separately. For data at day 7, the IFN-γ^+ IL-2^+/IFN-γ^+ TNF-α^+/IFN-γ^+ IL-2^+ TNF-α^+ were combined as "IFN^+ Multi" due to relatively lower percentage of these cells in some donors expressing double positive cytokines.

Statistical methods

All values with error bars are reported as mean ± SEM. Statistical analysis was performed using GraphPad Prism. Unpaired two-tailed *t*-test was used to evaluate statistical significances between two groups. Where indicated, paired two-tailed *t*-test

was used to compare the differences between two groups that combined data of different donors together.

DATA AND CODE AVAILABILITY

The data that support the findings of this study can be made available by the corresponding author. There is no customized code for this work. The set of adjustable parameters in GateID program has been indicated in the Methods section.